

See discussions, stats, and author profiles for this publication at: <https://www.researchgate.net/publication/338952983>

A Finite Element Framework for Magneto-Actuated Large Deformation and Instability of Slender Magneto-Active Elastomers

Article in *International Journal of Applied Mechanics* - January 2020

DOI: 10.1142/S1758825120500131

CITATIONS

2

READS

261

4 authors, including:



Yin Liu

King Abdullah University of Science and Technology

34 PUBLICATIONS 340 CITATIONS

[SEE PROFILE](#)



Shoue Chen

Michigan State University

13 PUBLICATIONS 73 CITATIONS

[SEE PROFILE](#)



Changyong Cao

Michigan State University

61 PUBLICATIONS 1,045 CITATIONS

[SEE PROFILE](#)

Some of the authors of this publication are also working on these related projects:



Quantum Dot lasers and VCSEL [View project](#)



Dynamic pull-in instability and snap-through buckling of initially curved microbeams under the effect of squeeze film damping, mechanical shock and axial force [View project](#)

A Finite Element Framework for Magneto-Actuated Large Deformation and Instability of Slender Magneto-Active Elastomers

Yin Liu^{*}, Shoue Chen^{*}, Xiaobo Tan[†]
and Changyong Cao^{*,†,‡}

^{}Laboratory for Soft Machines & Electronics
School of Packaging, Michigan State University
East Lansing, MI 48824, USA*

*[†]Departments of Electrical & Computer Engineering
Mechanical Engineering, Michigan State University
East Lansing, MI 48824, USA*

[‡]cca@msu.edu

Received 13 December 2019

Revised 19 December 2019

Accepted 20 December 2019

Published 26 March 2020

In this paper, we present an efficient finite element framework for modeling the finite deformations of slender magneto-active elastomers (MAE) under applied magnetic fields or currents. For the convenience of numerical modeling, magnetic field is defined at fixed spatial coordinates in the background space rather than in the elastic MAEs using material coordinates. The magnetic field will vary with free or localized currents while the spatial distribution of the magnetic field will evolve with the motion or deformation of the MAE materials, which is actuated by the surface or body forces induced by external magnetic fields or equivalent currents. A staggered strategy and a Riks method are introduced to solve the strongly coupled governing equations of the magnetic field and displacement field using finite element method. The mesh distortion along the interfaces between MAE domain and free-space domain is resolved by considering concurrent deformation of the mesh in these two domains. A few 2D numerical examples demonstrate the validity and efficiency of the developed model for simulating large deformation of MAE with non-uniform spatial magnetic field under different actuation sources such as free currents, magnetization or external magnetic field. This framework offers a new solution strategy for modeling mechano-magneto problems of MAEs and will help rational design and analysis of MAE-based actuators and soft robotics in the future.

Keywords: Magneto-active elastomer; smart materials; continuum theory; finite element method; mechano-magnetic interaction; soft robotics.

[‡]Corresponding author.

1. Introduction

Magneto-active elastomers (MAEs) are soft polymeric materials embedded with magnetically responsive particles (such as iron particles or tiny permanent magnets) or carried with free currents, which respond to external magnetic fields by producing large deformations or varying mechanical properties. They have been increasingly used for many emerging applications such as soft robotics [Hu *et al.*, 2018], printed untethered soft origami [Kim *et al.*, 2018], magnetically anisotropic micro actuators [Kim *et al.*, 2011], bistable switches [Hou *et al.*, 2018] and magnetoactive acoustic metamaterials [Yu *et al.*, 2018]. Recent advances in manipulating soft matter through magnetic fields have been reviewed in literature [Erb *et al.*, 2016]. Compared with other kinds of soft active materials like hydrogels and shape memory polymers, MAEs are able to generate fast response and deformation under an applied magnetic field, achieving a contactless and remote controlling.

The coupling behaviors of MAE have been extensively studied for a few decades [Eringen and Maugin, 2012; Pao, 1978; Pao and Hutter, 1975]. In most theories, the governing equations are developed based on the balance laws in the mechanical and magnetic fields, including the balance equations of linear momentum, moment of momentum and work in the mechanical field and the Gauss law and the Ampere's law in magnetostatics. The critical challenge for the mechanical-magnetic coupling problem is to derive the densities of force, couple, and work applied on the MAE by a magnetic field. A few methods have been developed to efficiently resolve this issue, such as the two dipole model for polarization and magnetization [Pao and Hutter, 1975], homogenization on force, couple and work on atomistic composites [Eringen and Maugin, 2012; Pao and Hutter, 1975], combination of the magnetic force into "long-range" and "short-range" terms [Brown, 1966], balance of energy [Kankanala and Triantafyllidis, 2004; Kovetz, 2000], as well as a direct calculation based on the magnetic force and couple on currents [Dorfmann and Ogden, 2016]. A detailed comparison and remark on the different forms of these terms can refer to Pao's review paper [Pao, 1978]. It has been widely accepted that the magnetic force in the balance equation can be transformed to the divergence of a Maxwell stress [Danas, 2017; Kankanala and Triantafyllidis, 2004; Metsch *et al.*, 2016] or a ponderomotive stress [Pelteret *et al.*, 2016; Vogel *et al.*, 2014]. Recently, several numerical approaches have been proposed to solve the coupled governing equations of mechanical and magnetic fields, using either commercial software [Bustamante *et al.*, 2011; Han *et al.*, 2013; Pelteret *et al.*, 2016] or in-house FE codes [Miehe *et al.*, 2016] and even a coupled BEM-FEM method [Nedjar, 2017]. The developed theories and numerical models have been utilized to study various behaviors of MAE, including the instability of a bilayer magnetoelastic film-substrate system [Danas and Triantafyllidis, 2014], the tunable stiffness of anisotropic MREs with column-chain magnetoactive particles [Rudykh and Bertoldi, 2013], fast-response magneto-sensitive hydrogels [Liu *et al.*, 2018a,b] iron-particle-filled magnetorheological elastomers [Danas *et al.*, 2012], rate-dependent magneto-active polymers

[Haldar *et al.*, 2016], as well as the nonlinear magnetization behavior of particles [Metsch *et al.*, 2016].

On the other hand, a few representative experiments have been conducted to verify the developed theories and numerical methods. For example, Zhao *et al.* performed the experiment demonstration and proposed a model for simulating MAE with hard-magnets embedded in an uniform magnetic field [Zhao *et al.*, 2019]. Psarra *et al.* investigated the surface instability of a film-substrate system under external stimuli of magnetic and mechanical fields [Psarra *et al.*, 2017]. Some research has explored the governing equations of MAE based on the minimization principle of free energy function [Ethiraj and Miehe, 2016; Liu, 2014; Miehe *et al.*, 2016], in which the Euler-Lagrange equations were derived on the condition of its first variation with respect to state variables vanished. However, choosing a specific form of free energy function and its related state variables remains controversial because the selected one may not be able to characterize the real free energy of the problem and then induce spurious results [Liu, 2014], which is crucial to obtaining admissible field equations. In addition, Han *et al.* [2011, 2013] developed an energy approach similar to the principle of virtual work and employed it to study the field-stiffening effect of MAEs under an external magnetic field. Recently, these theories have been extended to the homogenization scheme and are applied to model the macroscopic response of MAE with microstructures formed by microparticles of different sizes and distributions [Danas, 2017; Javili *et al.*, 2013; Keip and Rambausek, 2015; Ponte Castañeda and Galipeau, 2011; Zabihyan *et al.*, 2018]. On the basis of the homogenization scheme, the magneto-mechanical problem on the specimen scale has been studied in comparison with experimental results [Keip and Rambausek, 2017].

In most of the studies mentioned above, although the different definitions of Maxwell stress have been utilized, the balance equations of the linear momentum and the moment of momentum in mechanical field are overall consistent. Nevertheless, the constitutive equations they employed in the formulations are different and even controversial. One critical assumption in these works is that the magnetic induction depends on the deformation gradient, i.e., when the material is deformed, the magnetic induction will be changed, leading to a two-point first-order tensor. Actually, there are two parts in the free energy: the mechanical energy and the magnetic energy [Danas, 2017], both of which are the functions of the deformation gradient and the magnetic induction (or magnetic field). Thus, the Cauchy stress is dependent on both deformation gradient and magnetic flux. This results in a confusing inference that non-magneto-active materials (e.g., plastic and wood, no currents and no magnetization) will generate residual stresses when subjected to a magnetic field even if no mechanical force is applied on the materials. Furthermore, because the stress depends on the magnetic flux, it is challenging to explain the physical meanings of the boundary conditions. These controversies in the theoretical aspects may cause some difficulties in developing robust numerical models, such

as a unified approach for dealing with surface and body currents and magnetization, numerical deficiency due to mesh distortion at the interface of different domains, and barriers of extending the model to the pull-in instability problems. In addition, though modeling strong magneto-mechanical interaction of block MAE has been done in above mentioned works, rare applications for large bending of slender MAE were reported due to the challenge for handling mesh distortion near the interface between MAE and free space. The widely existing snap-through and pull-in instabilities in MAE structures were rarely studied within the finite element framework. It is of great importance to resolve these issues to help achieve a deep understanding of the coupled mechano-magneto behavior of MAEs and facilitate the rational design of soft robotics with MAEs.

In this work, we develop a robust finite element solution framework to model strong magneto-mechanical interaction in MAE, which attempts to model magneto-actuated large deformation and instability behaviors of slender MAEs within both uniform and non-uniform magnetic fields. In the theoretical aspect, for the convenience of numerical modeling, we assume the magnetic induction to be an Eulerian quantity, which is defined at fixed spatial coordinates in the background space rather than a two-point tensor. In this regard, the derived Cauchy stress is expressed as a function of the deformation gradient, similar to hyperplastic solids. The magnetic forces induced by spatial magnetic induction and free or localized currents are the driving force for the deformation of the elastic body. Conversely, current location and current density vary with the deformation of the MAE and thus cause a re-distribution of the magnetic induction. Therefore, the mechanical responses and magnetic fields are strongly coupled and intertwined with one another. Starting from the weak form of the balance equations, we have developed a staggered scheme and a Riks solution scheme to solve the coupled finite element (FE) formulation, where the displacements and magnetic vector potential are introduced as unknowns. The former one allows the fast verification of the efficiency of the model, while the latter one can be employed to solve the more challenging snap-through and pull-in instability problems in mechano-magnetic analysis. The mesh distortion near the interface between free space and MAE, due to large deformation of MAE, is handled by simulating concurrent mesh deformation in both MAE and free space. Analysis on several 2D beam-like MAE structures were performed to demonstrate its capability to predict large deformation of MAE and concurrent evolution of non-uniform magnetic field. To our knowledge, among the existing literatures, our model should be capable to handle the largest deformation degree along with non-uniform magnetic field distribution in slender MAE structures.

This paper is organized as follows. In Sec. 2, a modified continuum theory to model the strongly coupling mechano-magnetic behaviors of MAE is presented. The force, couple and work induced by the magnetic field on an arbitrary volume are derived and the balance laws in both mechanical and magnetic fields are summarized. Then, a staggered strategy and a Riks-based finite element procedure are

developed to solve the governing equations in Sec. 3, including the weak forms, linearization and FE discretization of the governing equations. The details for dealing with the mesh distortion along the interfaces between free space and MAE domain are addressed. In Sec. 4, a few representative examples are presented to demonstrate the validity of the proposed framework and methods to predict the coupling large deformations of MAEs as well as the variations of the magnetic field. Finally, summary and conclusion are given in Sec. 5.

2. Continuum Theory and Formulations

To simplify the derivation and analysis, in the following sections, we will ignore the heat and mass transfer inside the MAE domain, and calculate the magnetic induction in a background space. Thus, the magnetic induction is defined as a Eulerian (or spatial) quantity at a fixed point in the background space while the elastic deformation of body is defined as a Lagrangian (or material) quantity at a solid material point. With these assumptions included, the magnetic induction will not directly depend on the deformations of the body in the models. The detailed theory and formulations of the problem are presented as below.

2.1. Kinematics

In a coupled mechano-magnetic problem, the entire solution domain \mathcal{B} is composed of a free-space subdomain \mathcal{B}^f and the MAE domain \mathcal{B}^m (Fig. 1), i.e., $\mathcal{B} = \mathcal{B}^f \cup \mathcal{B}^m$. The assemble of MAE material points in the reference and current configurations are given as $\{\mathbf{y} | \mathbf{y} = \mathbf{x}, \mathbf{x} \in \mathcal{B}_R^m\}$ and $\{\mathbf{z} | \mathbf{z} = \mathbf{x}, \mathbf{x} \in \mathcal{B}^m\}$, respectively, where \mathbf{x} is the coordinate of an arbitrary point in the global coordinate system, \mathbf{y} and \mathbf{z} are the coordinates of MAE points in the reference configuration \mathcal{B}_R^m and the current

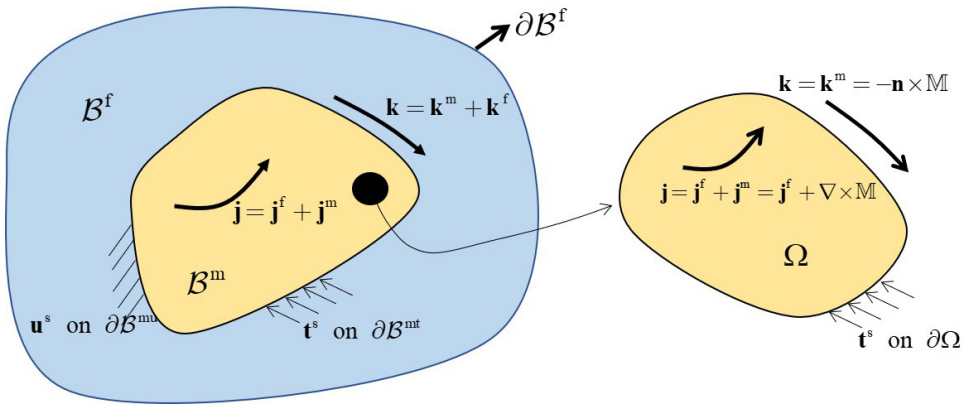


Fig. 1. Schematic illustration of the solution domains and boundary conditions for a representative MAE problem. \mathcal{B}^f denotes the free space, \mathcal{B}^m stands for the MAE domain, and $\mathcal{B} = \mathcal{B}^f \cup \mathcal{B}^m$ is the entire domain for the question.

configuration \mathcal{B}^m , respectively. For simplification, we respectively define the gradient operators with respect to \mathcal{B} , \mathcal{B}_R^m , and \mathcal{B}^m as

$$\nabla(\cdot) = \frac{\partial(\cdot)}{\partial x_i} \mathbf{e}_i, \quad \nabla^R(\cdot) = \frac{\partial(\cdot)}{\partial y_i} \mathbf{e}_i, \quad \nabla^C(\cdot) = \frac{\partial(\cdot)}{\partial z_i} \mathbf{e}_i \quad (1)$$

Since the elastic body is embedded in the background space, we have the following relations

$$\nabla(\cdot) = \nabla^R(\cdot), \quad \text{in } \mathcal{B}_R^m, \quad \text{and} \quad \nabla(\cdot) = \nabla^C(\cdot), \quad \text{in } \mathcal{B}^m \quad (2)$$

A one-to-one mapping from \mathcal{B}_R^m to \mathcal{B}^m for a specific material point at time t can be defined as $\mathbf{z} = \mathbf{z}(\mathbf{y}, t)$. Then, the deformation gradient is defined as $\mathbf{F} = \partial \mathbf{z} / \partial \mathbf{y} = \nabla^R \mathbf{z}$. Thus, the volume element dv and area element da in \mathcal{B}_R^m and \mathcal{B}^m are expressed as

$$d\mathbf{v} = J d\mathbf{v}_R, \quad n d\mathbf{a} = J \mathbf{F}^{-T} \mathbf{n}_R da_R \quad (3)$$

where $J = \det \mathbf{F}$ is the Jacobian, \mathbf{n} is the outer normal of the area element da and the quantities with subscripts ‘R’ refer to those in the reference configuration. The right Cauchy-Green strain and the Green strain can be respectively defined as $\mathbf{C} = \mathbf{F}^T \mathbf{F}$ and $\mathbf{E} = \frac{1}{2}(\mathbf{C} - \mathbf{I})$, where \mathbf{I} is the identity tensor. The velocity gradient and its symmetrical part are given as

$$\mathbf{l} = \partial \mathbf{v} / \partial \mathbf{z} = \nabla^C \mathbf{v}, \quad \mathbf{d} = \frac{1}{2}(\mathbf{l} + \mathbf{l}^T) \quad (4)$$

2.2. Magnetostatics

In the basic equations of magnetostatics, we consider the total currents as free currents and localized currents arising from magnetization, which are respectively represented as body currents inside the MAE and surface currents on its boundary. Such a treatment has been adopted in literature by Brown [1966], in which he categorized the forces in a magnetic field into three different types as “*forces exerted by current circuits on current circuits, forces exerted by magnetized bodies on magnetized bodies, and forces exerted by current circuits on magnetized bodies or vice versa*”. He also illustrated the equivalence between the density of magnetic moment (magnetization) and body and surface currents, which was also employed in electrodynamic analysis by Jackson [1999].

In our model, since mechanical deformation has no direct influence on magnetic induction \mathbb{B} , we can express \mathbb{B} as a function of the coordinates in the background space, i.e., $\mathbb{B} = \mathbb{B}(\mathbf{x})$, and ignore the relation of \mathbb{B} in different configurations.¹ The governing equations for magnetostatics in \mathcal{B} are then expressed as

$$\nabla \cdot \mathbb{B} = 0, \quad \nabla \times \mathbb{B} = \mu_0 \mathbf{j} \quad (5)$$

¹In most previous literatures, \mathbb{B} is expressed as $\mathbb{B} = J^{-1} \mathbf{F} \mathbb{B}_R$, where \mathbb{B}_R is the magnetic induction in the reference configuration.

and the boundary conditions are

$$\begin{cases} \mathbf{n} \cdot \llbracket \mathbb{B} \rrbracket = 0, & \mathbf{n} \times \llbracket \mathbb{B} \rrbracket = \mu_0 \mathbf{k} & \text{on } \partial \mathcal{B}^m \\ \mathbb{B} = \mathbf{0} & & \text{on } \partial \mathcal{B}^f \end{cases} \quad (6)$$

where \mathbf{j} and \mathbf{k} are the total body current density inside \mathcal{B}^m and the surface current density on $\partial \mathcal{B}^m$, respectively. $\mu_0 = 4\pi \times 10^{-7}$ H/m is the permeability in free space and $\llbracket \cdot \rrbracket = [\cdot]^{\text{out}} - [\cdot]^{\text{in}}$ denotes jump conditions on $\partial \mathcal{B}^m$. With a magnetic vector potential \mathbb{A} , the corresponding magnetic induction can be expressed as

$$\mathbb{B} = \nabla \times \mathbb{A} \quad (7)$$

For an isotropic MAE, the constitutive equation is given as

$$\mathbb{B} = \mu_0(\mathbb{H} + \mathbb{M}) \quad (8)$$

where \mathbb{H} and \mathbb{M} are magnetic intensity and magnetization. Then, the total body current density in Eq. (5) can be rewritten as

$$\mathbf{j} = \mathbf{j}^f + \mathbf{j}^m \quad (9)$$

where the localized and free currents densities are, respectively, expressed as

$$\mathbf{j}^m = \nabla \times \mathbb{M} = \nabla^C \times \mathbb{M} \quad \text{and} \quad \mathbf{j}^f = \nabla \times \mathbb{H} = \nabla^C \times \mathbb{H} \quad (10)$$

Similarly, the total surface current density satisfies

$$\mathbf{k} = \mathbf{k}^f + \mathbf{k}^m = \mathbf{n} \times \llbracket \mathbb{H} \rrbracket + \mathbf{n} \times \llbracket \mathbb{M} \rrbracket \quad (11)$$

A similar treatment on \mathbb{M} as equivalent currents \mathbf{j}^m and \mathbf{k}^m was employed in previous studies [Brown, 1966; Jackson, 1999].

Remark 1. Though the magnetic induction \mathbb{B} at the spatial point does not change with the deformation, this is not true for the magnetization and the currents in the elastic body. The localized currents generated from magnetization should be affected by the deformation. Therefore, following previous work, the relation between currents in different configurations are given as

$$\mathbf{j} = J^{-1} \mathbf{F} \mathbf{j}_R, \quad \mathbf{k} = \mathbf{F}^{-T} \mathbf{k}_R \quad (12)$$

where the quantities with subscripts “ R ” refer to those in \mathcal{B}_R^m . The magnetizations in different configurations are related by $\mathbb{M}_R = \mathbf{F}^T \mathbb{M}$, and it is proved that

$$\mathbf{j}_R^m = \nabla^R \times \mathbb{M}_R \quad (13)$$

Remark 2. From Eqs. (10) and (12), the localized body current \mathbf{j}^m vanishes in both reference and current configurations, i.e., $\mathbf{j}_R^m = \mathbf{j}^m = \mathbf{0}$, in a uniform magnetization field. The localized surface current can be calculated by $\mathbf{k}^m = \mathbf{n} \times \llbracket \mathbb{M} \rrbracket$ and can be rewritten as $\mathbf{k}^m = -\mathbf{n} \times \mathbb{M}^{\text{in}}$ due to no magnetization in the free space, where \mathbb{M}^{in} is the magnetization of MAE on $\partial \mathcal{B}^m$. These relations can be used to simplify the

magnetization in MAE as equivalent currents, like the cases of permanent magnets or soft ferromagnetic particles.

2.3. Force, couple and work applied by magnetic field

In this section, we consider magnetic force, couple and work of an arbitrary volume element Ω of MAE in Fig. 1. The governing equations for magnetostatics in Ω are expressed as

$$\begin{cases} \nabla \cdot \mathbb{B} = 0, & \nabla \times \mathbb{B} = \mu_0 \mathbf{j} \\ \mathbf{n} \cdot \mathbb{B} = \mathbf{n} \cdot \mathbb{B}^{\text{out}}, & \mathbf{n} \times \mathbb{B} = -\mu_0 \mathbf{k}^{\text{m}} \end{cases} \quad \text{on } \partial\Omega \quad (14)$$

where \mathbb{B}^{out} is the prescribed magnetic induction on the boundary $\partial\Omega$. Due to the presence of the surface and body currents, \mathbf{k}^{m} and \mathbf{j} , the magnetic field exerts Ampere's forces on Ω , which can be expressed as

$$\mathbf{f}^{\text{m}} = \int_{\partial\Omega} \mathbf{k}^{\text{m}} \times \mathbb{B} da + \int_{\Omega} \mathbf{j} \times \mathbb{B} dv \quad (15)$$

with the relation $\mathbf{k}^{\text{m}} = -\mathbf{n} \times \mathbb{M}$ and integrating the term of surface integration by part, we can obtain

$$\mathbf{f}^{\text{m}} = \int_{\Omega} \nabla^{\text{C}} \cdot (-\mathbb{M} \otimes \mathbb{B} + (\mathbb{M} \cdot \mathbb{B})\mathbf{I}) + \mathbf{j} \times \mathbb{B} dv \quad (16)$$

Furthermore, considering $\nabla \times \mathbb{B} = \mu_0 \mathbf{j}$ in Eq. (5), \mathbf{f}^{m} can be further expressed as

$$\mathbf{f}^{\text{m}} = \int_{\Omega} \nabla^{\text{C}} \cdot (-\mathbb{M} \otimes \mathbb{B} + (\mathbb{M} \cdot \mathbb{B})\mathbf{I}) + \frac{1}{\mu_0} (\mathbb{B} \otimes \mathbb{B}) - \frac{1}{2\mu_0} (\mathbb{B} \cdot \mathbb{B})\mathbf{I} dv \quad (17)$$

or

$$\mathbf{f}^{\text{m}} = \int_{\Omega} \mathbf{j}^{\text{f}} \times \mathbb{B} + (\nabla \mathbb{B})^{\text{T}} \mathbb{M} dv \quad (18)$$

It is noted that Eqs. (17) and (18) have been obtained by different methods in previous research [Eringen and Maugin, 2012; Maugin, 2013] and widely accepted as the magnetic force applied on a volume element of MAE [Dorfmann and Ogden, 2016]. Similarly, for the magnetic couple on Ω , we obtain

$$\mathbf{c}^{\text{m}} = \int_{\partial\Omega} \mathbf{x} \times (\mathbf{k}^{\text{m}} \times \mathbb{B}) da + \int_{\Omega} \mathbf{x} \times (\mathbf{j} \times \mathbb{B}) dv \quad (19)$$

Integrating the first term on the right hand by parts leads to

$$\mathbf{c}^{\text{m}} = \int_{\Omega} \mathbf{x} \times [\text{div}(-\mathbb{M} \otimes \mathbb{B} + (\mathbb{M} \cdot \mathbb{B})\mathbf{I}) + \mathbf{j} \times \mathbb{B}] + \mathbb{M} \times \mathbb{B} dv \quad (20)$$

The work of magnetic field in the domain Ω can be divided into two parts: one done by magnetic force and the other one induced by the change of magnetic flux. The

work done by the magnetic force on a velocity field \mathbf{v} can be calculated as

$$\begin{aligned}
 \dot{w}^{m1} &= \int_{\partial\Omega} (\mathbf{k}^m \times \mathbb{B}) \cdot \mathbf{v} \, da + \int_{\Omega} (\mathbf{j} \times \mathbb{B}) \cdot \mathbf{v} \, dv \\
 &= \int_{\Omega} [\mathbf{j} \times \mathbb{B} + \operatorname{div}(-\mathbb{M} \otimes \mathbb{B} + (\mathbb{M} \cdot \mathbb{B})\mathbf{I})] \cdot \mathbf{v} \, dv \\
 &\quad + \int_{\Omega} [-\mathbb{M} \otimes \mathbb{B} + (\mathbb{M} \cdot \mathbb{B})\mathbf{I}] : \mathbf{l} \, dv
 \end{aligned} \tag{21}$$

where \mathbf{v} is assumed to be very small in the quasi-static case considered in this work. To get the work (or energy change) by the change of magnetic flux, we multiply $\nabla \times \mathbb{B} = \mu_0 \mathbf{j}$ in (14) with $\dot{\mathbb{A}}$ and integrate it by part over the domain Ω , thus obtaining

$$\int_{\Omega} \dot{\mathbb{A}} \cdot (\nabla \times \mathbb{B}) \, dv = \int_{\Omega} \dot{\mathbb{B}} \cdot \mathbb{B} \, dv - \int_{\partial\Omega} \mu_0 \dot{\mathbb{A}} \cdot \mathbf{k}^m \, da = \int_{\Omega} \mu_0 \dot{\mathbb{A}} \cdot \mathbf{j} \, da \tag{22}$$

The boundary conditions in Eq. (14) and the relation $\dot{\mathbb{B}} = \nabla \times \dot{\mathbb{A}}$ are used in the derivation of the above equation. If we ignore the body charge term in the Faraday's law, i.e., $\nabla \times \mathbb{E} + \dot{\mathbb{B}} = \mathbf{0}$, with \mathbb{E} the electrical intensity, it will have $\mathbb{E} = -\dot{\mathbb{A}}$ after using $\dot{\mathbb{B}} = \nabla \times \dot{\mathbb{A}}$. Thus, Eq. (22) can be rewritten as

$$\int_{\Omega} \frac{1}{\mu_0} \dot{\mathbb{B}} \cdot \mathbb{B} \, dv = - \int_{\partial\Omega} \mathbb{E} \cdot \mathbf{k}^m \, da - \int_{\Omega} \mathbb{E} \cdot \mathbf{j} \, da \tag{23}$$

It is found that Eq. (23) can be reduced to the Poynting's theorem in the case of $\mathbf{k}^m = \mathbf{0}$ if the energy change from the electrical field is ignored. The terms on the right hand can be interpreted as “generalized work” done by the external (equivalent) currents, while the one on the left hand is the energy change of the magnetic field. Thus, the second part of the work can be expressed as

$$\dot{w}^{m2} = \int_{\Omega} \frac{1}{\mu_0} \mathbb{B} \cdot \dot{\mathbb{B}} \, dv \tag{24}$$

This energy change in magnetic field is the same as that in the free space derived by Jackson [1999]. It is noted that the integration domain Ω for Eqs. (22)–(24) is the background space, although it overlaps the same spatial points as the elastic body (see Eq. (21)). Therefore, \dot{w}^{m2} cannot be included in the balance law of the energy in the elastic body.

Based on above derivations, we can define the energy density of the magnetic field as

$$\psi^m = \frac{1}{2\mu_0} \mathbb{B} \cdot \mathbb{B} \tag{25}$$

and the corresponding constitutive equation

$$\mathbb{M} + \mathbb{H} = \frac{\mathbb{B}}{\mu_0} = \frac{\partial \psi^m}{\partial \mathbb{B}} \tag{26}$$

Here the magnetic induction and energy itself have no direct relation with the elastic deformation, and thus disappear in the constitutive equation for the Cauchy stress.

2.4. Balance laws in the mechanical field

In this section, we consider the balance law in the domain Ω for the mechanical field. By ignoring the inertial effect, the integral form of the balance of linear momentum is given as

$$\mathbf{f}^m + \int_{\Omega} \mathbf{f}^b \, dv + \int_{\partial\Omega} \mathbf{t}^s \, da = \mathbf{0} \quad (27)$$

where \mathbf{f}^b and $\mathbf{t}^s = \boldsymbol{\sigma}_s^T \mathbf{n}$ are, respectively, the body force per unit volume and the surface traction, and $\boldsymbol{\sigma}_s$ is a stress tensor caused by surface traction. Using Eq. (16) and integrating the terms related to $\partial\Omega$ in Eq. (27) by part, the local form of balance of linear momentum can be obtained as

$$\operatorname{div} \boldsymbol{\sigma}^T + \mathbf{f}^b + \mathbf{j} \times \mathbb{B} = \mathbf{0} \quad (28)$$

where $\boldsymbol{\sigma}^T = \boldsymbol{\sigma}_s^T - \mathbb{M} \otimes \mathbb{B} + (\mathbb{M} \cdot \mathbb{B}) \mathbf{1}$ is the Cauchy stress. It is noted that, for the convenience of later use, the effects of the magnetic body force $\mathbf{j} \times \mathbb{B}$ are not included in the Cauchy stress. It can be easily verified that $\boldsymbol{\sigma}^T \mathbf{n} = \mathbf{t}^s + \mathbf{k}^m \times \mathbb{B}$, where the summation in the right-hand side represents the total surface traction from both mechanical and magnetic fields.

Using Eqs. (20) and (28), the integral form and local form of the balance of momentum are respectively expressed as

$$\mathbf{c}^m + \int_{\Omega} \mathbf{x} \times \mathbf{f}^b \, dv + \int_{\partial\Omega} \mathbf{x} \times \mathbf{t}^s \, da = \mathbf{0} \quad (29)$$

and

$$\mathcal{E} : \boldsymbol{\sigma}_s^T + \mathbb{M} \times \mathbb{B} = \mathbf{0} \Leftrightarrow \mathcal{E} : \boldsymbol{\sigma}^T = \mathbf{0} \Leftrightarrow \boldsymbol{\sigma} = \boldsymbol{\sigma}^T \quad (30)$$

where \mathcal{E} is the three-dimensional Levi-Civita symbol, and the Cauchy stress $\boldsymbol{\sigma}$ is symmetric. From Eqs. (21)–(24), the balance of energy in Ω for the elastic body can be given as

$$\frac{d}{dt} \int_{\Omega} \psi \, dv = \dot{w}^{m1} + \int_{\Omega} \mathbf{f}^b \cdot \mathbf{v} \, dv + \int_{\partial\Omega} \mathbf{t}^s \cdot \mathbf{v} \, da \quad (31)$$

where Ψ the strain energy at an arbitrary material point of the elastic body in Ω . Combining the balance equations in Eqs. (28) and (30), its local form can be derived as

$$\dot{\Psi}_R = \mathbf{P} : \dot{\mathbf{F}} \quad (32)$$

where $\Psi_R = J\Psi$ is the strain energy density in \mathcal{B}_R^m , and $\mathbf{P} = \frac{1}{J} \boldsymbol{\sigma} \mathbf{F}^T$ is the first Piola-Kirchhoff stress. The physical meaning of Eqs. (31) and (32) is the same as the classical theory of mechanics of hyperelastic solids, i.e., the work done by the

total external forces is equal to the change of the total strain energy of the material. Therefore, the constitutive equation for the deformation field can be defined as

$$\mathbf{P} = \frac{\partial \psi_{\mathbb{R}}}{\partial \mathbf{F}} \quad (33)$$

The energy change in the mechanical and magnetic fields, i.e., Eqs. (25) and (32), are independent of each other due to the previous assumptions for \mathbb{B} , thus \mathbf{P} is not directly related to \mathbb{B} . This constitutive framework is similar to the one developed by Kalina *et al.* [2016] for modeling the coupled mechano-magnetic behaviors of a linearly elastic MAE. Therefore, based on above derivations, the governing equations for the MAE problem shown in Fig. 1 can be presented as follows:

$$\text{mechanical field : } \begin{cases} \nabla^C \boldsymbol{\sigma}^T + \mathbf{f}^b + \mathbf{j} \times \mathbb{B} = \mathbf{0}, & \boldsymbol{\sigma} = \boldsymbol{\sigma}^T \quad \text{in } \mathcal{B}^m \\ \boldsymbol{\sigma} = J \frac{\partial \psi_{\mathbb{R}}}{\partial \mathbf{F}} \mathbf{F}^{-T} \\ \mathbf{u} = \mathbf{u}^s \quad \text{on } \partial \mathcal{B}^{mu} \\ \boldsymbol{\sigma} \mathbf{n} = \mathbf{t}^s + \mathbf{k} \times \mathbb{B} \quad \text{on } \partial \mathcal{B}^m \end{cases} \quad (34)$$

and

$$\text{magnetic field : } \begin{cases} \mathbb{B} = \nabla \times \mathbb{A}, & \nabla \times \mathbb{B} = \mu_0 \mathbf{j} \\ \mathbf{n} \cdot [\mathbb{B}] = 0, & \mathbf{n} \times [\mathbb{B}] = \mu_0 \mathbf{k}, \quad \text{on } \partial \mathcal{B}^m \\ \mathbb{A} = \bar{\mathbb{A}}, & \text{on } \partial \mathcal{B}^f \end{cases} \quad (35)$$

where \mathbf{u}^s is the prescribed displacement on $\partial \mathcal{B}^{mu}$, \mathbf{t}^s is the mechanical surface traction, $\mathbf{k} = \mathbf{k}^f + \mathbf{k}^m$ is the total surface current consisting of the free current \mathbf{k}^f and the magnetization current $\mathbf{k}^m = -\mathbf{n} \times \mathbb{M}$. From Eqs. (34) and (35), it can be concluded that, in modelling MAE, the magnetic forces on the body and the surface currents deform the elastic body, while the deformation of MAE in turn changes the location and the magnitude of induced currents as well as the redistribution of magnetic flux in the background space.

Remark 3. The surface current \mathbf{k}^f should exist in the surface electromagnetic conductor (e.g., conductive wires or electrode on $\partial \mathcal{B}^m$), and thus a magnetic force $\mathbf{k}^f \times \mathbb{B}$ will exert on its surface, rather than directly on \mathcal{B}^m . However, we ignore the stiffness of the surface conductor in this work, and thus $\mathbf{k}^f \times \mathbb{B}$ can be treated as a force applied directly on \mathcal{B}^m .

Remark 4. Equation (35) is applicable to the cases with a prescribed \mathbb{M} , e.g., a MAE with embedded hard-magnets. However, for materials with “soft” ferromagnet particles (e.g., annealed iron), \mathbb{M} is induced in the magnetizing process by external magnetic field. If we use a linear relation $\mathbb{M} = \chi \mathbb{H}$, where χ is magnetic susceptibility, based on Eq. (8), we can obtain $\mathbb{B} = \mu_0 \mu \mathbb{H}$ and $\mathbb{M} = \frac{\mu-1}{\mu_0} \mathbb{B}$, where $\mu = 1 + \chi$ is

the relative permeability. Thus, the Ampere's law in magnetostatics will become $\nabla \times \mathbb{B} = \mu\mu_0\mathbf{j}^f$ in this case.

3. Implementation of Finite Element Method

3.1. Weak form and linearization

The weak form for the governing equations Eq. (34) in the mechanical field can be expressed as

$$\begin{aligned}
 \delta W_1 &= - \int_{\mathcal{B}^m} (\nabla^C \boldsymbol{\sigma}^T + \mathbf{f}^b + \mathbf{j} \times \mathbb{B}) \cdot \delta \mathbf{u} \, dv \\
 &= \underbrace{\int_{\mathcal{B}^m} \boldsymbol{\sigma} : \delta \mathbf{d} \, dv}_{\delta W_{1,\text{int}}} \\
 &\quad - \underbrace{\int_{\mathcal{B}^m} (\mathbf{f}^b + \mathbf{j} \times \mathbb{B}) \cdot \delta \mathbf{u} \, dv - \int_{\partial \mathcal{B}^m t} \mathbf{t}^s \cdot \delta \mathbf{u} \, da - \int_{\partial \mathcal{B}^m} (\mathbf{k} \times \mathbb{B}) \cdot \delta \mathbf{u} \, da}_{\delta W_{1,\text{ext}}}
 \end{aligned} \tag{36}$$

where $\delta \mathbf{u}$ is the virtual displacement, and $\delta \mathbf{d} = \frac{1}{2}(\delta \mathbf{l} + \delta \mathbf{l}^T)$ with $\delta \mathbf{l} = \nabla^C \delta \mathbf{u}$. This equation is almost the same as the one for classical hyperelasticity, except for the terms related to the magnetic forces on the currents in $\delta W_{1,\text{ext}}$. The internal virtual work can be alternatively expressed in the reference configuration as

$$\delta W_{1,\text{int}} = \int_{\mathcal{B}^m} \boldsymbol{\sigma} : \delta \mathbf{d} \, dv = \int_{\mathcal{B}_R^m} \mathbf{P} : \delta \mathbf{F} \, dv_R \tag{37}$$

Ignoring the linearization terms related to $\delta W_{1,\text{ext}}$, the increment form of δW_1 follows:

$$\Delta \delta W_1 = \Delta \delta W_{1,\text{int}} = \int_{\mathcal{B}_R^m} \Delta \mathbf{F} : \mathbb{C} : \delta \mathbf{F} \, dv_R \tag{38}$$

where $\Delta \mathbf{F} = \nabla^R(\Delta \mathbf{u})$, $\delta \mathbf{F} = \nabla^R(\delta \mathbf{u})$, $\Delta \mathbf{u}$ is the increment of the displacement vector, and \mathbb{C} is the forth-order tangent modulus

$$\mathbb{C} = \frac{\partial^2 \psi_R}{\partial \mathbf{F} \otimes \partial \mathbf{F}} \tag{39}$$

Using Eq. (7), the virtual work equation for the governing equation Eq. (35) in a magnetic field becomes

$$\delta W_2 = \underbrace{\int_{\mathcal{B}} \frac{1}{\mu_0} \delta \mathbb{B} \cdot \mathbb{B} \, dv}_{\delta W_{2,\text{int}}} - \underbrace{\int_{\mathcal{B}} \delta \mathbb{A} \cdot \mathbf{j} \, dv - \int_{\partial \mathcal{B}} \delta \mathbb{A} \cdot \mathbf{k} \, da}_{\delta W_{2,\text{ext}}} \tag{40}$$

It should be noted that the integration in Eq. (40) is performed in the background space.

Remark 5. Ignoring the mechanical loads, body current \mathbf{j} , and free surface current \mathbf{k}^f , Eq. (36) can be reduced as

$$\int_{\mathcal{B}^m} [\boldsymbol{\sigma} + \mathbb{M} \otimes \mathbb{B} - (\mathbb{M} \cdot \mathbb{B})\mathbf{I}] : \delta \mathbf{l} - \operatorname{div}(-\mathbb{M} \otimes \mathbb{B} + (\mathbb{M} \cdot \mathbb{B})\mathbf{I}) \cdot \mathbf{v} \, dv = 0 \quad (41)$$

Considering the relations $\nabla \times \mathbb{M} = \mathbf{0}$ and $\nabla \cdot \mathbb{B} = \mathbf{0}$, it can be verified that $\operatorname{div}(-\mathbb{M} \otimes \mathbb{B} + (\mathbb{M} \cdot \mathbb{B})\mathbf{I}) = \mathbf{0}$, and thus we can obtain

$$\int_{\mathcal{B}^m} [\boldsymbol{\sigma} + \mathbb{M} \otimes \mathbb{B} - (\mathbb{M} \cdot \mathbb{B})\mathbf{I}] : \delta \mathbf{l} \, dv = 0 \quad (42)$$

In this case, with $\boldsymbol{\sigma} = J\mathbf{P}\mathbf{F}^{-T}$ and Eq. (33), we can define an equivalent stress as

$$\boldsymbol{\sigma}^{\text{eqv}} = J \frac{\partial \psi_R}{\partial \mathbf{F}} \mathbf{F}^{-T} + \mathbb{M} \otimes \mathbb{B} - (\mathbb{M} \cdot \mathbb{B})\mathbf{I} \quad (43)$$

with which we may be able to develop a simplified computation scheme with a prescribed \mathbb{B} .

Remark 6. When the magnetization \mathbb{M} is generated from magnetizable soft ferromagnets, rather than permanent magnets, based on Remark 4, Eq. (40) should be revised as

$$\delta W_2 = \int_{\mathcal{B}} \frac{1}{\mu\mu_0} \delta \mathbb{B} \cdot \mathbb{B} \, dv - \int_{\mathcal{B}} \delta \mathbb{A} \cdot \mathbf{j}^f \, dv - \int_{\partial \mathcal{B}} \delta \mathbb{A} \cdot \mathbf{k}^f \, da \quad (44)$$

3.2. Discretization

In the FE discretization, the entire domain \mathcal{B} is assumed to be discretized into n_e elements, i.e.,

$$\mathcal{B} = \mathcal{B}^m \cup \mathcal{B}^f = \left(\bigcup_{e=1}^{n_e^m} \mathcal{B}_e^m \right) \cup \left(\bigcup_{e=1}^{n_e^f} \mathcal{B}_e^f \right) \quad (45)$$

where n_e^m and n_e^f are the total element number in MAE and free-space domains, respectively, and have the relation of $n_e = n_e^m + n_e^f$. The interpolation of displacement vector and vector potential on an element can be expressed as

$$\delta \mathbf{u}^h = \sum_{i=1}^{n_d} \mathbf{N}_{ui} \delta \mathbf{u}_i, \quad \Delta \mathbf{u}^h = \sum_{i=1}^{n_d} \mathbf{N}_{ui} \Delta \mathbf{u}_i \quad (46)$$

$$\delta \mathbb{A}^h = \sum_{i=1}^{n_d} \mathbf{N}_{Ai} \delta \mathbb{A}_i, \quad \mathbb{A}^h = \sum_{i=1}^{n_d} \mathbf{N}_{Ai} \mathbb{A}_i \quad (47)$$

where \mathbf{N}_{ui} and \mathbf{N}_{Ai} are interpolation functions corresponding to node i for displacement and vector potential fields, $\delta \mathbf{u}_i$ and $\Delta \mathbf{u}_i$ are the virtual and incremental displacement of node i , $\delta \mathbb{A}_i$ and \mathbb{A}_i are the virtual and total vector potential of node i , and n_d is the total node number of the element.

The vector forms related to the gradient of displacement and the curl of vector potential are written as

$$(\nabla^R \delta \mathbf{u})^h = \sum_{i=1}^{n_d} \mathbf{B}_{ui} \delta \mathbf{u}_i, \quad (\nabla^R \Delta \mathbf{u})^h = \sum_{i=1}^{n_d} \mathbf{B}_{ui} \Delta \mathbf{u}_i \quad (48)$$

$$(\nabla \times \delta \mathbb{A})^h = \sum_{i=1}^{n_d} \mathbf{B}_{Ai} \delta \mathbb{A}_i, \quad (\nabla \times \mathbb{A})^h = \sum_{i=1}^{n_d} \mathbf{B}_{Ai} \mathbb{A}_i \quad (49)$$

where \mathbf{B}_{ui} and \mathbf{B}_{Ai} are generalized strain matrix consisting of the derivatives of \mathbf{N}_{ui} and \mathbf{N}_{Ai} , respectively. Substituting Eqs. (46) and (48) into Eqs. (36) and (37), we can obtain the discretized balance equation in the mechanical field in \mathcal{B}^m ,

$$\begin{aligned} \mathbf{R} = \mathbf{f}^{\text{int}} - \mathbf{f}^{\text{ext}} = \mathcal{A}_{e=1}^{n_e} \int_{\mathcal{B}_{eR}^m} \mathbf{B}_u^T \mathbf{P} dv_R \\ - \mathcal{A}_{e=1}^{n_e} \left(\int_{\mathcal{B}_e^m} \mathbf{N}_u^T (\mathbf{f}^b + \mathbf{j} \times \mathbb{B}) dv + \int_{\partial \mathcal{B}_e^m} \mathbf{N}_u^T (\mathbf{t}^s + \mathbf{k} \times \mathbb{B}) da \right) \end{aligned} \quad (50)$$

where \mathcal{A} denotes the assembly operator, \mathcal{B}_{eR}^m is the reference domain of the element \mathcal{B}_e^m . Using Eqs. (38) and (48), the increment equation in the mechanical field can be expressed as

$$\mathbf{K}_t \Delta \mathbf{u} = -\mathbf{R} \quad (51)$$

where the tangent stiffness matrix can be expressed as

$$\mathbf{K}_t = \mathcal{A}_{e=1}^{n_e} \int_{\mathcal{B}_{eR}^m} \mathbf{B}_u^T \mathbf{D}_u \mathbf{B}_u dv_R \quad (52)$$

and the constitutive matrix \mathbf{D}_u is composed of the elements of \mathbb{C} in Eq. (39), which is the same as that for classical hyperelastic materials.

For the discretized governing equation in the magnetic field in \mathcal{B} , using Eqs. (40), (47) and (49), we can obtain

$$\mathbf{K}_g \mathbb{A} = \mathbf{J}_g \quad (53)$$

where the stiffness matrix and the generalized force are respectively expressed as

$$\mathbf{K}_g = \mathcal{A}_{e=1}^{n_e} \int_{\mathcal{B}_e} \frac{1}{\mu_0} \mathbf{B}_A^T \mathbf{B}_A dv, \quad \mathbf{J}_g = \mathcal{A}_{e=1}^{n_e} \left(\int_{\mathcal{B}_e} \mathbf{N}_A^T \mathbf{j} dv + \int_{\partial \mathcal{B}_e} \mathbf{N}_A^T \mathbf{k} da \right) \quad (54)$$

In the next section, we discuss how to solve the discretized governing equations numerically.

3.3. Staggered solution scheme and mesh distortion

From the weak forms in Eqs. (36) and (44), it is found that the two physical fields interact with each other via the magnetic forces and the variation of location and magnitude of currents. Thus, it is suitable to use a staggered solution scheme to solve

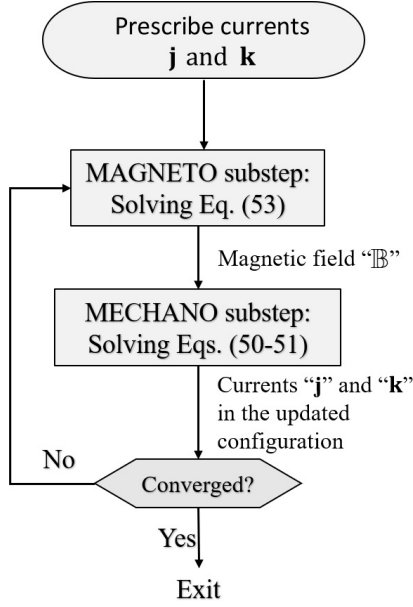


Fig. 2. Flowchart for the iteration process of the proposed staggered solution scheme in one load step.

the governing equations of MAEs. As shown in Fig. 2, in the iteration process of one load step, a fixed increment of current is first given as generalized external loads, and then the magnetic induction can be solved based on Eq. (53) in the MAGNETO substep. After obtaining the updated magnetic flux at the Gauss and nodal points, the external force \mathbf{f}^{ext} on the right-hand side of Eq. (50) is then updated, and a new equilibrium configuration of \mathcal{B} can be calculated using the Newton-Raphson scheme in the MECHANO substep. The iteration continues until the results converge based on the required criterion. The detailed iteration procedures are given in Table 1. It should be noted that the error indicator e_A for the staggered iteration differs from that e_u in the MECHANO substep, and are, respectively, defined as

$$e_A = \|\mathbb{A}^{s,t} - \mathbb{A}^{s,t-1}\| / \|\mathbb{A}^{s,t-1}\|, \quad e_u = \|\Delta \mathbf{u}^{\text{adj}}\| / \|\mathbf{u}\| \quad (55)$$

where s and t are the load step number and staggered step number (see Table 1), respectively, and $\Delta \mathbf{u}^{\text{adj}}$ are displacement increment of two adjacent steps in the Newton-Raphson scheme in the MECHANO substep, while \mathbf{u} is the total displacement. In the following examples, the tolerances for e_A and e_u are taken as 10^{-6} .

It is noted that the solution domains \mathcal{B}^m and \mathcal{B} for the weak forms Eqs. (36) and (44) in the two fields are not compatible with each other. The material domain \mathcal{B}^m will change its shape in the deformation process while the free space domain \mathcal{B}^f will not. This incompatibility will result in the gaps or penetrations along the interface between the domain \mathcal{B}^m and the domain \mathcal{B}^f . The remeshing approach in the free

Table 1. Flowchart of the proposed staggered iterative scheme in one load step.

-
- (a) Start load step s : prescribe increments of (free or localized) currents, $\Delta \mathbf{j}^s$ and $\Delta \mathbf{k}^s$, update the currents in the current load step, $\mathbf{j}^{s-1} + \Delta \mathbf{j}^s \rightarrow \mathbf{j}^s$, set the iteration step $t = 1$;
 - (b) MAGNETO substep: Solve Eq. (53) for fixed \mathbf{j}^s and \mathbf{k}^s in the current configuration $\mathcal{B}^{s,t-1}$, obtain $\mathbb{A}^{s,t}$ at each node, calculate $\mathbb{B}^{s,t}$ at each Gauss point, and extrapolate $\mathbb{B}^{s,t}$ from Gauss points to nodal points;
 - (c) MECHANO substep: Calculate the magnetic force using \mathbf{j}^s , \mathbf{k}^s and $\mathbb{B}^{s,t}$, iteratively solve the equilibrium equation in Eqs. (50) and (51), obtain the total incremental displacement $\Delta \mathbf{u}^{s,t}$ for prescribed currents \mathbf{j}^s and \mathbf{k}^s using the Newton-Raphson Scheme, and update nodal coordinates $\mathbf{x}^{s,t-1} + \Delta \mathbf{u}^{s,t} = \mathbf{x}^{s,t}$ and stress $\boldsymbol{\sigma}^{s,t}$ in the new configuration $\mathcal{B}^{s,t}$;
 - (d) If $e_A > e_{A,\text{Tot}}$, the results are not converged, let $t = t + 1$, start another round of iteration, and go to step (b); Otherwise, the results are converged, let $\mathbf{x}^{s,t} \rightarrow \mathbf{x}^{s+1,0}$, $\mathbb{A}^{s,t} \rightarrow \mathbb{A}^{s+1,0}$, $\mathbb{B}^{s,t} \rightarrow \mathbb{B}^{s+1,0}$, $s = s + 1$ and go to the next load step (a).
-

space [Pelletier *et al.*, 2016] may be used to deal with such a problem, however, it should be very time-consuming and even technically tricky.

To resolve this problem, a much larger size of free space domain \mathcal{B}^f is introduced in the model and discretized by deformable meshes and is assumed to have a negligible elastic or shear modulus (e.g., 10^{-10} times of the modulus of MAE). This treatment enables us to model the coupling mechano-magnetic behaviors of MAEs without obviously affecting the calculated results in both fields. The relatively tiny stiffness added in the free space has negligible influence on the deformation of the elastic body, and the relatively large size of the free space \mathcal{B}^f in the model ensures the calculated accuracy for the magnetic flux around \mathcal{B}^m even if the shape of domain \mathcal{B} changes in the deformation. Consequently, the integration domain in the virtual work, Eq. (36), has to be extended to the entire solution domain \mathcal{B} , while the displacement boundary conditions are still imposed on $\partial \mathcal{B}^{mu}$ as usual. Because the free space deforms with the elastic body, the mesh quality near to $\partial \mathcal{B}^m$ will be automatically adjusted in the numerical simulation, so as to avoid severe mesh distortions when large deformations occur in the elastic body.

To overcome the possible near singularity of the stiffness matrix caused by the extremely small stiffness of the free space, the governing equation Eq. (51) is reformulated in a block form as

$$\underbrace{\begin{bmatrix} \mathbf{K}_{mm} & \mathbf{K}_{mf} \\ \mathbf{K}_{fm} & \mathbf{K}_{ff} \end{bmatrix}}_{\mathbf{K}^m} \underbrace{\begin{Bmatrix} \Delta \mathbf{u}_m \\ \Delta \mathbf{u}_f \end{Bmatrix}}_{\Delta \mathbf{u}} = - \underbrace{\begin{Bmatrix} \mathbf{R}_m \\ \mathbf{R}_f \end{Bmatrix}}_{\mathbf{R}} \quad (56)$$

where $\Delta \mathbf{u}_m$ and $\Delta \mathbf{u}_f$ are displacement increments in the MAE and the free space, respectively, and \mathbf{R}_m and \mathbf{R}_f are the corresponding unbalance forces. The magnitude of the elements in \mathbf{K}_{mm} should be much larger than \mathbf{K}_{ff} , because the stiffness of the elastic body is much larger than that of the free space assigned with a small digit. The equation for solving $\Delta \mathbf{u}_m$ can be obtained by

$$(\mathbf{K}_{mm} - \mathbf{K}_{mf} \mathbf{K}_{ff}^{-1} \mathbf{K}_{fm}) \Delta \mathbf{u}_m = -\mathbf{R}_m + \mathbf{K}_{mf} \mathbf{K}_{ff}^{-1} \mathbf{R}_f \quad (57)$$

It can be easily observed that the elements in new stiffness matrix $\mathbf{K}_{mm} - \mathbf{K}_{mf} \mathbf{K}_{ff}^{-1} \mathbf{K}_{fm}$ have almost the same order magnitude and thus it is well conditioned. Therefore, the issue of near singularity of \mathbf{K}^m is resolved.

3.4. The Riks method

To apply the Riks method to solve the governing equation, \mathbf{j} and \mathbf{k} are decomposed into a fixed part and a variable part,

$$\mathbf{j} = \mathbf{j}_f + \mathbf{j}_v = \mathbf{j}_f + \alpha \mathbf{j}_p, \quad \mathbf{k} = \mathbf{k}_f + \mathbf{k}_v = \mathbf{k}_f + \alpha \mathbf{k}_p \quad (58)$$

where \mathbf{j}_f and \mathbf{k}_f are the fixed parts of currents which do not change in the simulation, \mathbf{j}_v and \mathbf{k}_v are variable parts of currents which are generally expressed as the product of a scalar α and corresponding fixed pattern \mathbf{j}_p and \mathbf{k}_p . In this scheme, α becomes a generalized load factor. Because we employed a linear constitutive equation Eq. (8) in the magnetic field, the vector potential and the magnetic flux can be decomposed as

$$\mathbb{A} = \mathbb{A}_f + \alpha \mathbb{A}_p \quad (59)$$

$$\mathbb{B} = \mathbb{B}_f + \alpha \mathbb{B}_p \quad (60)$$

where \mathbb{A}_f and \mathbb{B}_f are fixed parts caused by \mathbf{j}_f and \mathbf{k}_f , and \mathbb{A}_p and \mathbb{B}_p are their patterns induced by \mathbf{j}_p and \mathbf{k}_p .

For brevity, the external force in Eq. (50) is written as

$$\bar{\mathbf{f}}[\mathbf{j}, \mathbf{k}, \mathbb{B}] = \mathcal{A}_{e=1}^{nem} \left(\int_{\mathcal{B}_e^m} \mathbf{N}_u^T (\mathbf{j} \times \mathbb{B}) dv + \int_{\partial \mathcal{B}_e^m} \mathbf{N}_u^T (\mathbf{k} \times \mathbb{B}) da \right) \quad (61)$$

Then, based on Eqs. (58)–(60), the external force caused by the magnetic field in Eq. (50) can be expressed as a fixed part $\mathbf{f}_f^{\text{ext}}$ and a variable part $\mathbf{f}_v^{\text{ext}}$

$$\mathbf{f}^{\text{ext}} = \mathbf{f}_f^{\text{ext}} + \mathbf{f}_v^{\text{ext}} \quad (62)$$

where

$$\mathbf{f}_f^{\text{ext}} = \bar{\mathbf{f}}[\mathbf{j}_f, \mathbf{k}_f, \mathbb{B}_f] \quad (63)$$

$$\mathbf{f}_v^{\text{ext}} = \alpha (\bar{\mathbf{f}}[\mathbf{j}_p, \mathbf{k}_p, \mathbb{B}_p] + \bar{\mathbf{f}}[\mathbf{j}_f, \mathbf{k}_f, \mathbb{B}_p]) + \alpha^2 \bar{\mathbf{f}}[\mathbf{j}_p, \mathbf{k}_p, \mathbb{B}_p] \quad (64)$$

The increment of \mathbf{f}^{ext} can be calculated as

$$\Delta \mathbf{f}^{\text{ext}} = \Delta \alpha (\bar{\mathbf{f}}[\mathbf{j}_p, \mathbf{k}_p, \mathbb{B}_p] + \bar{\mathbf{f}}[\mathbf{j}_f, \mathbf{k}_f, \mathbb{B}_p]) + 2\alpha \Delta \alpha \bar{\mathbf{f}}[\mathbf{j}_p, \mathbf{k}_p, \mathbb{B}_p] = \Delta \alpha \bar{\mathbf{f}}_v^{\text{ext}} \quad (65)$$

where the force pattern vector is $\bar{\mathbf{f}}_v^{\text{ext}} = \bar{\mathbf{f}}[\mathbf{j}_p, \mathbf{k}_p, \mathbb{B}_p] + \bar{\mathbf{f}}[\mathbf{j}_f, \mathbf{k}_f, \mathbb{B}_p] + 2\alpha \bar{\mathbf{f}}[\mathbf{j}_p, \mathbf{k}_p, \mathbb{B}_p]$.

Therefore, in the Riks solution framework, the incremental equation for Eq. (51) is modified as

$$\mathbf{K}^m \Delta \mathbf{u} = -\mathbf{R} + \Delta \alpha \bar{\mathbf{f}}_v^{\text{ext}} \quad (66)$$

Table 2. The flowchart of the Riks solution scheme in a load step.

-
- (a) Start load step . . . , and set the iteration step $q = 1$;
 - (b) MAGNETO substep: Solve Eq. (53) for given fixed currents \mathbf{j}_f and \mathbf{k}_f and pattern currents \mathbf{j}_p and \mathbf{k}_p to obtain $\mathbb{A}_f^{r,s}$ and $\mathbb{A}_p^{r,s}$ at each node; calculate $\mathbb{B}_f^{r,s}$ and $\mathbb{B}_p^{r,s}$ at each Gauss point, and extrapolate them from Gauss points to nodal points.
 - (c) MECHANO substep: Calculate the stiffness matrix $\mathbf{K}_t^{s,t}$, the unbalanced force $\mathbf{R}^{s,t}$ the magnetic pattern force $(\bar{\mathbf{f}}_v^{\text{ext}})^{s,t}$ based on results at iteration step t . Solve Eqs. (66) and (67) to obtain $\Delta \mathbf{u}^{s,t}$ and $\Delta \alpha^{s,t}$; Update nodal coordinates $\mathbf{x}^{s,t-1} + \Delta \mathbf{u}^{s,t} \rightarrow \mathbf{x}^{s,t}$ and stress $\boldsymbol{\sigma}^{s,t}$ in $\mathcal{B}^{s,t}$ and update the scalar factor $\alpha^{s,t-1} + \Delta \alpha^{s,t} \rightarrow \alpha^{s,t}$ and magnetic flux using Eqs. (59) and (60).
 - (d) If $e_A > e_{A,\text{Tot}}$, the results are not converged, let $t = t + 1$, and go to step (b) to start another iteration; Otherwise, the results are converged, let $\mathbf{x}^{s,t} \rightarrow \mathbf{x}^{s+1,0}$, $\mathbb{A}^{s,t} \rightarrow \mathbb{A}^{s+1,0}$, $\mathbb{B}^{s,t} \rightarrow \mathbb{B}^{s+1,0}$, $\alpha^{s,t} \rightarrow \alpha^{s+1,0}$, $s = s + 1$ to start the next load step.
-

To solve the Eq. (66), an arc-length equation related to $\Delta \mathbf{u}$ and $\Delta \alpha$ is introduced as

$$\Delta \mathbf{u} \cdot \Delta \mathbf{u} + \xi \Delta \alpha^2 = \rho^2 \quad (67)$$

where ρ is the arc length that controls the step size in the calculation, and ξ is a scaling parameter. Here, ξ is taken as zeros.

The detailed iteration procedures for the Riks scheme to solve this problem are presented in Table 2. The error indicator e_A is defined as

$$e_A = \|\mathbb{A}^{s,t} - \mathbb{A}^{s,t-1}\| / \|\mathbb{A}^{s,t-1}\| \quad (68)$$

where s and t are the load step number and iteration step number, respectively. Other issues in the Riks solution scheme, such as automatic adjustment of ρ and selection strategy of $\Delta \alpha$ can refer to our previous work [Liu *et al.*, 2017].

3.5. Specification in 2D cases

For two-dimensional (2D) problems, the solution framework can be simplified in a (x, y) coordinate system. The vector potential is reduced to $\mathbb{A} = \mathbb{A}_z \mathbf{k}$, where \mathbf{k} is a unit vector perpendicular to the x - y plane. The magnetic flux becomes

$$\mathbb{B}_x = \frac{\partial \mathbb{A}_z}{\partial y}, \quad \mathbb{B}_y = -\frac{\partial \mathbb{A}_z}{\partial x} \quad (69)$$

If neo-Hookean model is utilized to describe the mechanical constitutive relation of the materials, the strain energy function can be expressed as

$$\psi_R = \frac{1}{2}G(\mathbf{C} - 3 - 2 \log J) + \frac{1}{2}K(J - 1)^2 \quad (70)$$

where G and K are the shear modulus and the bulk modulus, respectively. Using Eqs. (33) and (39), the stress and tangent modulus can be obtained as

$$\mathbf{P} = G(\mathbf{F} - \mathbf{F}^{-T}) + KJ(J - 1)\mathbf{F}^{-T} \quad (71)$$

$$\mathbb{C}_{ijkl} = G(\delta_{ik}\delta_{jl} + F_{jk}^{-1}F_{li}^{-1}) + (2J - 1)F_{ji}^{-1}F_{lk}^{-1} \quad (72)$$

Because the material is nearly incompressible, i.e., $K \gg G$, the F-bar method [de Souza Neto *et al.*, 1996] is employed to deal with the volumetric locking problem encountered in the analysis. A 2D quadrilateral element with bilinear interpolations for both displacement and vector potential fields is developed and used in our in-house codes.

4. Numerical Examples

In this section, we present a few 2D examples to demonstrate the efficiency of the solution framework for modeling the coupled mechano-magnetic behaviors of MAE, including a soft MAE bar with 1D elongation for verification, a cantilever MAE beam with body current in uniform magnetic field and two current-loading cantilever beams for large deformation in non-uniform magnetic field, and pull-in and snap-through instabilities of MAE beams for further demonstration. In these examples, non-dimensional data are used to present the results and unless specifically noted, we utilize the staggered solution scheme to solve the problem.

4.1. Elongation of a MAE bar

As shown in Fig. 3, a soft MAE bar with dimension $L_0 \times h_0 = 0.5 \times 0.05$ is placed in a uniform magnetic field $\bar{\mathbb{B}}_x$, where L_0 and h_0 are its initial length and thickness, respectively, and $\bar{\mathbb{B}}_x$ is parallel to the x axis. The displacements at $y = \frac{h_0}{2}$ in the y direction are constrained so that the bar only allows 1D elongation. Surface currents $-k_z \mathbb{k}$ and $k_z \mathbb{k}$ are applied at the top and bottom surfaces, which will generate a pressure on the beam due to the magnetic force induced by the magnetic field to elongate the beam along the x direction.

The magnetic flux near to the elastic bar can be assumed to be uniform and equal to $\bar{\mathbb{B}}_x$ in the case that $\bar{\mathbb{B}}_x$ is far larger than the magnetic flux produced by $-k_z \mathbb{k}$ and $k_z \mathbb{k}$. In this case, the deformation gradient becomes $\mathbf{F} = \text{diag}(\lambda, \frac{1}{\lambda})$ due to the material incompressibility, where $\lambda = L/L_0$ is the stretch ratio in the x

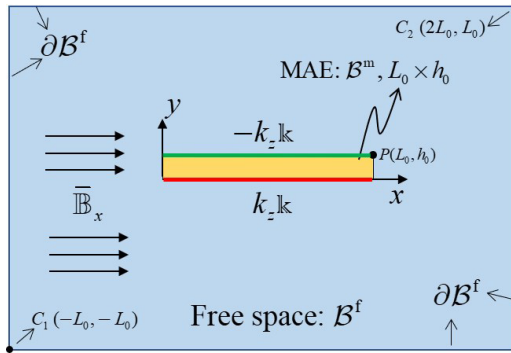


Fig. 3. Schematic of a soft MAE bar with surface current embedded in a uniform magnetic field.

direction, and L is the deformed length of the elastic beam. For the convenience of theoretical analysis, the strain energy function is modified as

$$\psi_R = \frac{1}{2}G(\mathbf{C} - 3 - 2 \log J) + p(J - 1) \quad (73)$$

where p is a Lagrange multiplier enforcing the incompressible condition of the material, then the Cauchy stress can be obtained as $\boldsymbol{\sigma} = G(\mathbf{F}\mathbf{F}^T - \mathbf{I}) + p\mathbf{I}$. Substituting \mathbf{F} into the constitutive equation, we can obtain the equilibrium equations

$$\begin{cases} G(\lambda^2 - 1) + p = 0 \\ G\left(\frac{1}{\lambda^2} - 1\right) + p = k_z \bar{\mathbb{B}}_x \end{cases} \quad (74)$$

After eliminating p in Eq. (74), it can be easily obtained that

$$\frac{1}{\lambda^2} - \lambda^2 = \frac{k_z}{G} \bar{\mathbb{B}}_x \quad (75)$$

Solving Eq. (75), we can obtain the relation between λ and the non-dimensional surface current $\frac{\bar{\mathbb{B}}_x}{G} k_z$.

In the FE simulation, the uniform magnetic field is applied by prescribing a vector potential at the boundary of the free space, $\partial\mathcal{B}^f$, as $\mathbb{A}_z = \omega y$, where y is the node coordinate at $\partial\mathcal{B}^f$ and ω is a scalar characterizing the magnitude of the magnetic flux. From Eq. (69), it is obtained $\bar{\mathbb{B}}_x = \omega$ if the magnetic field generated by the surface currents k_z is ignored. Three values of $\omega=1, 0.1$ and 0.05 are taken in the simulation. The final non-dimensional current $\frac{\omega}{G} k_z$ is fixed to be 2.0 and a total of 20 load steps with equal increments are used in the simulation.

The evolution of the stretch λ and the x -directional magnetic flux at the central point $O(\frac{L_0}{2}, \frac{h_0}{2})$ are shown in Figs. 4(a) and 4(b), and the distributions

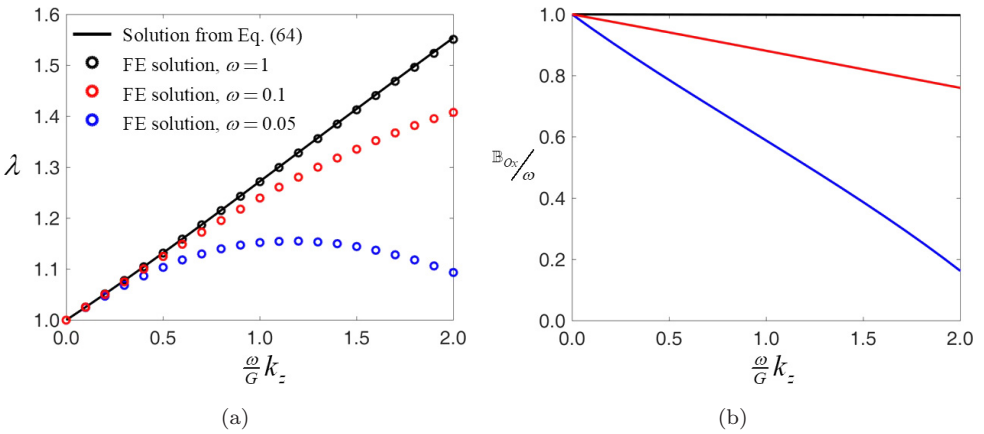


Fig. 4. Evolution of (a) the stretch λ and (b) the nominal magnetic flux \mathbb{B}_{Ox}/ω at the central point $O(\frac{L_0}{2}, \frac{h_0}{2})$ with respect to $\frac{\omega k_z}{G}$. Three values $\omega = 1, 0.1, 0.05$ of the external magnetic flux are considered.

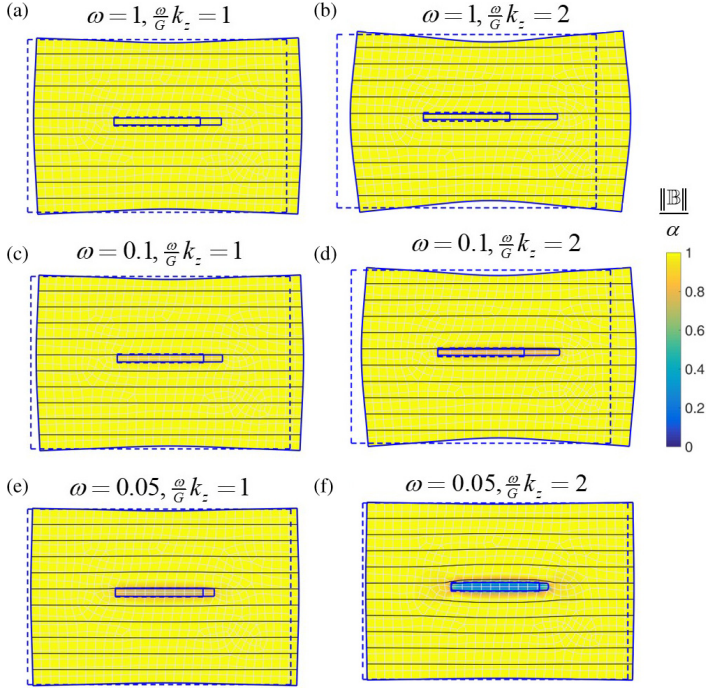


Fig. 5. Distribution of the magnitude of the magnetic flux $\|\mathbb{B}\|$ in the deformed configurations for different values of ω and k_z . The results are extracted at (a, c and e) middle load steps with current $\frac{\omega k_z}{G} = 1$ and (b, d and f) the last load steps with current $\frac{\omega k_z}{G} = 2$. It is noted that the solid dark lines inside the domain are the magnetic flux lines and the dash lines are the boundaries of the reference configurations. The deformed FE meshes are shown in a light gray color.

of magnitude of magnetic flux $\|\mathbb{B}\| = \sqrt{\mathbb{B}_x^2 + \mathbb{B}_y^2}$ at the final load step are given in Fig. 5. For a large external magnetic field with $\omega = 1$, the magnetic field produced by the surface current has little influence on the external one and thus $\|\mathbb{B}\|$ shows a uniform distribution across the entire domain with a value $\mathbb{B}_x = \omega = 1$ (Figs. 4(b) and 5(a)). In this case, the stretches obtained from the FE simulation and the analytical solution in Eq. (75) agree very well (Fig. 4(a), the black line and dots), which demonstrates the validity and accuracy of the developed FE model. For a smaller ω of 0.1 or 0.05, the FE solutions for λ deviate from the analytical one (Fig. 4(a)) because the surface currents significantly affect the external magnetic field (Figs. 4(b) and 5(b)–5(c)). The magnetic flux induced by the surface current has an opposite direction with the external magnetic field inside \mathcal{B}^m , leading to a decrease of the resulting magnetic field (Figs. 4(b) and 5(b)–5(c)). An interesting phenomenon for the case of $\omega = 0.05$ is that λ increases first and then decreases (Fig. 4(a)), indicating that the beam first elongates and then shortens as k_z increases. This is because the surface currents exert repulsive force with each other due to their opposite directions, and this repulsive force dominates for large k_z , leading to an expansion of the beam in the y direction and a shrinkage in the x direction.

From this example, several advantages of the proposed FE procedures in modeling MAE can be found: (1) The strong interaction between magnetic field and mechanical deformation is well characterized. For instance, in Fig. 5(c), localized changes of the magnetic flux in \mathcal{B}^m are captured for a small external magnetic field, while \mathbb{B} is maintaining uniformity in the free-space domain \mathcal{B}^f despite large deformation of the mesh, indicating the effectiveness of the method for applying the boundary condition of the magnetic field. (2) No mesh distortion problem exists in the free space (Figs. 5(b)–5(c), the deformed mesh) due to the automatic adjustment of the mesh in free-space along with MAE mesh. (3) The convergence speed is

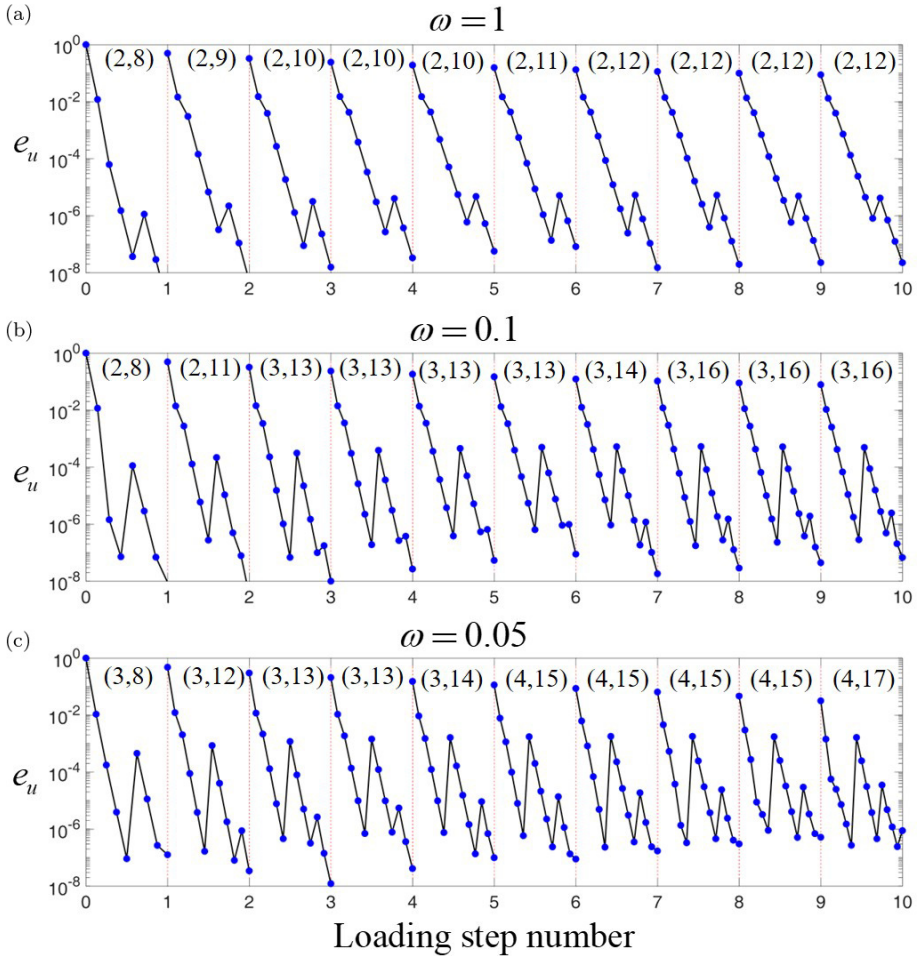


Fig. 6. Evolution of e_u in Eq. (58) in the first ten load steps for modeling the 1D elongation of the soft MAE bar with (a) $\omega = 1$, (b) $\omega = 0.1$ and (c) $\omega = 0.05$. The inserted numbers in each load step are the total numbers of the staggered steps and the iteration steps in the Newton-Raphson scheme of each MECHANO substep.

satisfying, especially for the case with larger values ($\omega = 1$). For instance, as shown in Fig. 6 for the evolution of e_u (Eq. (58)) in the first 10 load steps, it usually takes about 2 or 4 staggered iteration steps in a load step to reach converged results.

4.2. Bending of a cantilever beam

In this example, a cantilever beam made of soft MAE is considered, with the same dimension $L_0 \times h_0 = 0.5 \times 0.05$ as described in Example 4.1 (Fig. 3). A body current $j_z \mathbf{k}$ is applied onto the MAE beam, while its left end at $x = 0$ is clamped. Two different external magnetic fields $\omega = 0.02$ and 0.002 are considered. The beam will bend upward with the applied upward magnetic body force. In the FE simulation, the maximum value of $\frac{\omega}{G} j_z$ is set to 0.1 and twenty load steps with equal increment step size are used.

The evolution of non-dimensional displacement $\frac{u_{Py}}{L_0}$ and magnetic flux $\frac{\|\mathbb{B}_P\|}{\omega}$ at point P with the initial coordinate (L_0, h_0) are presented in Figs. 7(a) and 7(b),

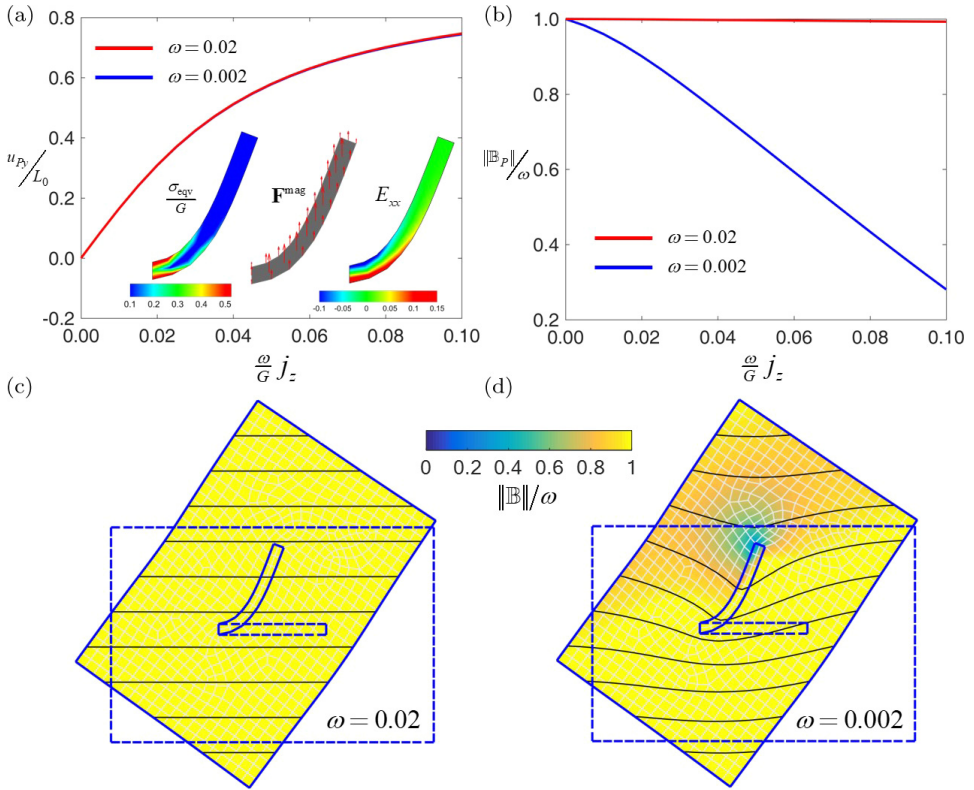


Fig. 7. Evolution of (a) the non-dimensional displacement and (b) magnitude of magnetic flux with respect to the body current. (c) and (d) are the deformed shapes and distribution of magnetic flux for different external magnetic field with $\omega = 0.02$ and 0.002 , respectively.

while the distributions of magnetic flux at the last load step are given in Figs. 7(c) and 7(d). The deformation shape in Fig. 7(c) qualitatively agree with the experiment results of a soft beam embedded with hard magnets in a uniform magnetic field [Zhao *et al.*, 2019]. It can be seen that for both cases, the large bending behaviors of the beam are well captured in the simulation and the non-dimensional Von Mises stress $\frac{\sigma^{eqv}}{G}$ and Green strain component E_{xx} are consistent with the results of the bending of a cantilever beam (Fig. 7(a)), where the maximum stress and strain are located at the top and bottom surface near to the clamped end. The magnetic force \mathbf{F}^{mag} distributing across the entire beam and along the upward direction is the actuation force for the bending of the beam. Though the mesh in free space shows a large rotation, it does not affect the uniform distribution of the external magnetic field when it is much larger than the one produced by the body current $j_z \mathbf{k}$ (Fig. 7(c)). For a smaller external magnetic field $\omega = 0.002$, it requires larger current in the elastic beam to reach the same degree of bending and the magnetic flux becomes non-uniform and both its direction and magnitude show spatial change (Fig. 7(d)). The magnetic flux at the tip of the beam decreases for a small ω while it remains a constant for a large ω (Fig. 7(b)), which is consistent with results in Figs. 7(c) and 7(d). With concurrent rotation of the mesh in both free space and MAE, this approach can well capture the variation of the magnetic field together with the large rotation of the beam without remeshing.

4.3. Interactions between a pair of MAE beams

As shown in Fig. 8, a pair of cantilever MAE beams are clamped on the wall, with an equivalent magnetic field generated through applying body currents j_z of same magnitude in the z direction. The geometry dimension of the beam is $L_0 \times h_0$, where $L_0 = \frac{50}{3}h_0$ and the distance between the two beams is $d_0 = \frac{20}{3}h_0$. Actuated by the magnetic force, the beams can bend upward or downward depending on the directions of the applied currents in the analysis [Jackson, 1999]. When opposite

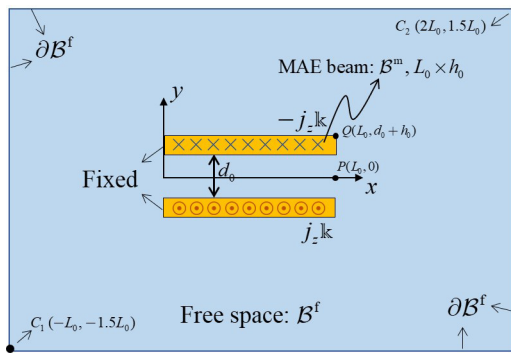


Fig. 8. Schematic plot of two parallel current-loading cantilever beams.

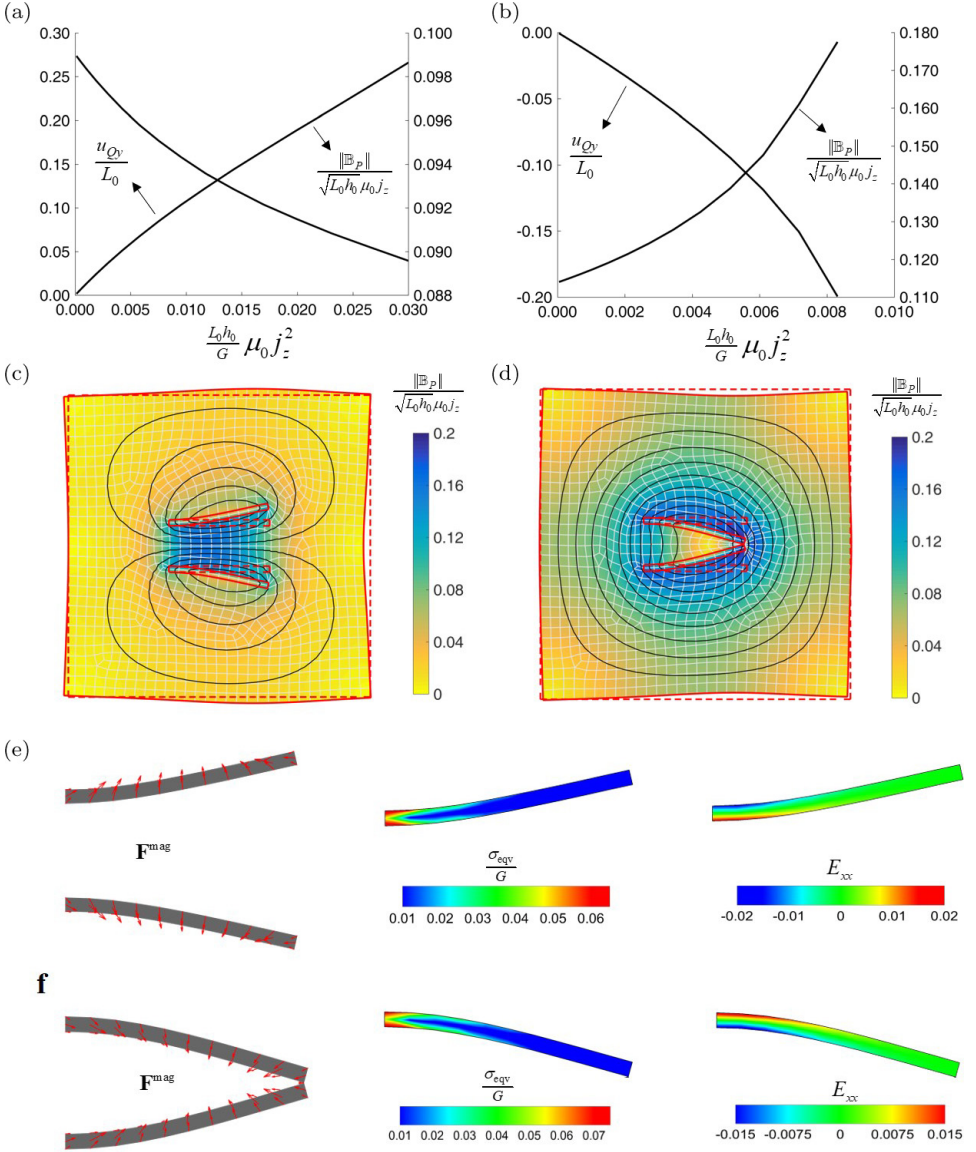


Fig. 9. (Color online) (a, b) Displacement at point Q and magnetic flux at point P as a function of the magnitude of applied currents in either opposite or same directions. (c, d) Contour plots of magnetic field in the deformed configuration. (e, f) The magnetic forces, Von Mises stresses, and Green strains in the two different cases.

directional currents are applied onto the two beams, they will repel each other and bend oppositely to the separating directions (Figs. 9(a) and 9(c)). As expected, the non-dimensional magnetic flux $\|\mathbb{B}_P\|/(\sqrt{L_0 h_0 \mu_0 j_z})$ at point P decreases with the applied current (Fig. 9(a)). It should remain a constant if the beams are composed

of a rigid conductor since $\|\mathbb{B}_P\|$ is proportional to j_z in this case. On the other hand, if the same directional currents are applied onto the beams, they will attract to each other (Fig. 9(d)) and the non-dimensional magnetic flux at point P will increase with j_z (Fig. 9(b)). It can be seen that the magnetic flux is not proportional to the applied current magnitude because of the deformations of the two beams. Thus, the deformation of the two beams has significant effect on the variation of the magnetic field. Also, due to concurrent adjustment of mesh shape in free space, no mesh distortion appears in the studied range of bending degree.

4.4. Interaction of a current-loading beam with an electromagnet

In this example, a cantilever beam with surface currents k_{zv} at its top and bottom surfaces is placed in a magnetic field generated by an electromagnet (Fig. 10) which is equivalent to surface current k_{zf} satisfying $k_{zf} = 10k_{zv}$. The dimension of the beam is $L_0 \times h_0$ with $L_0 = 10h_0$ and its distance to the top surface of the magnet is $d_0 = 0.5L_0$. In the FE simulation, two cases with different relative permeability in the MAE beam are considered, i.e., $\mu_r = 1$ and 100, which represent an ordinary deformable media and a magnetizable one, respectively. The electromagnet itself is assumed to be a rigid magneto-unresponsive material with an equivalent shear modulus 10^3 times larger than that of the beam.

Due to the interaction between the currents in the cantilever beam and electromagnet, the beams bend upward in both cases (Figs. 11(a) and 11(b)). The magnetic forces show opposite directions at the top and bottom surfaces (Figs. 11(c) and 11(d)), and the resulting force leads to an upward motion of the beam. Comparing the results in Figs. 11(a) and 11(b), the magnetic flux shows maximum value at different places, that is, for a higher permeability media in the beam, the magnetic flux is concentrated inside the beam (Fig. 11(b)), while the maximum value is found

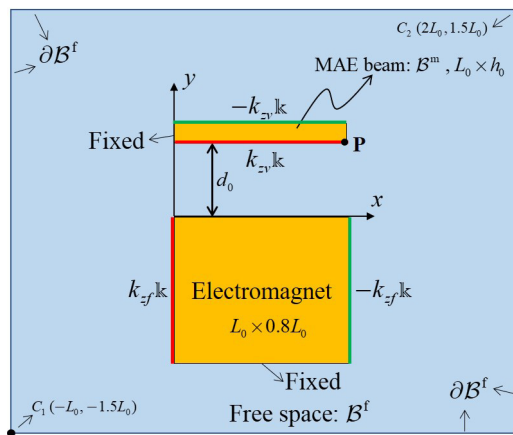


Fig. 10. Schematic of a current-loading cantilever beam and an electromagnet.

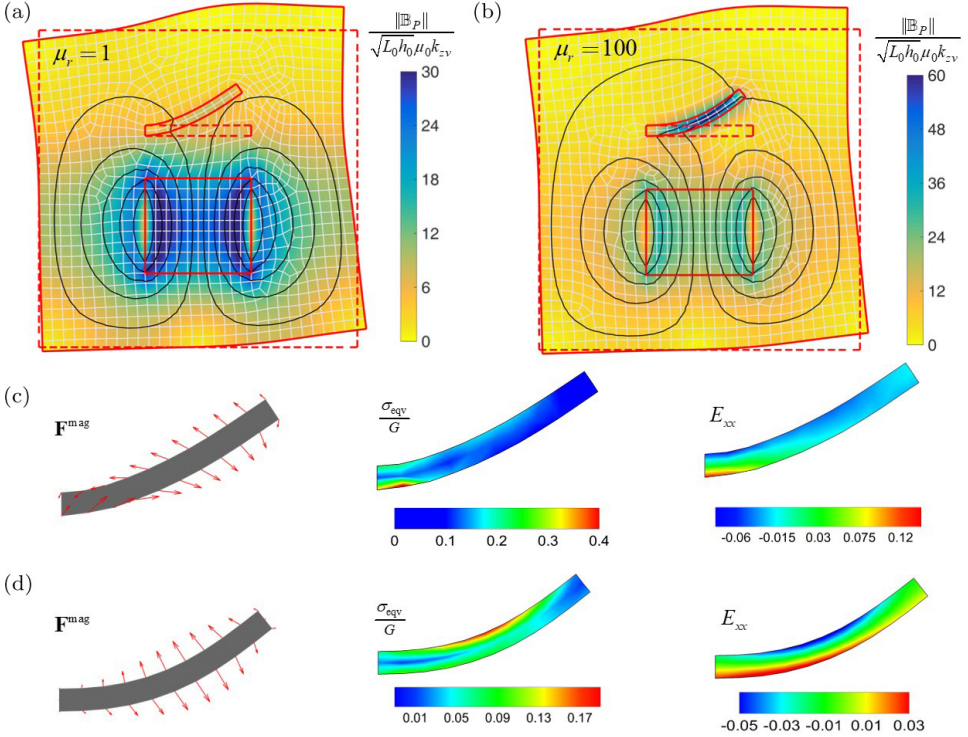


Fig. 11. Distribution of magnetic flux in the deformed configuration for different relative permeability of the beam (a) $\mu_r = 1$ and (b) $\mu_r = 100$. (c) and (d) are plots of the magnetic forces, Von Mises stress, and a component of Green strain in the beam for $\mu_r = 1$ and $\mu_r = 100$, respectively.

near the currents in the electromagnet for low permeability media. In addition, the stress and strain in the beam also show differences for the two cases. The maximum Von Mises stress for the case $\mu_r = 1$ is near the clamped end (Fig. 11(c)), but in the middle of its surface for the case $\mu_r = 100$ (Fig. 11(d)). This example also indicates that the mesh shape in the free space adjusts itself automatically in this numerical scheme, which allows for the superior modeling of the concurrent redistribution of the magnetic field and mechanical deformation without remeshing.

If the direction of surface current on the cantilever beam is changed, it bends downward and shows pull-in instability at a critical current, which means that the deflection of the beam abruptly increases due to the increasing attraction of the electromagnet. Here, we use the developed Riks solution scheme to solve the non-monotonic evolution of the equilibrium path. From Fig. 12(a) for the y -directional displacement at point P, it can be easily identified that the beam has pull-in instability at point A (see configuration in Fig. 12(b) if the current continues to increase. It means that at point A, the beam bends sharply to a large degree and jumps to another configuration which is attached to the electromagnet. Additionally, though the free-space mesh distorts severely at configuration B (Fig. 12(c)), the solution

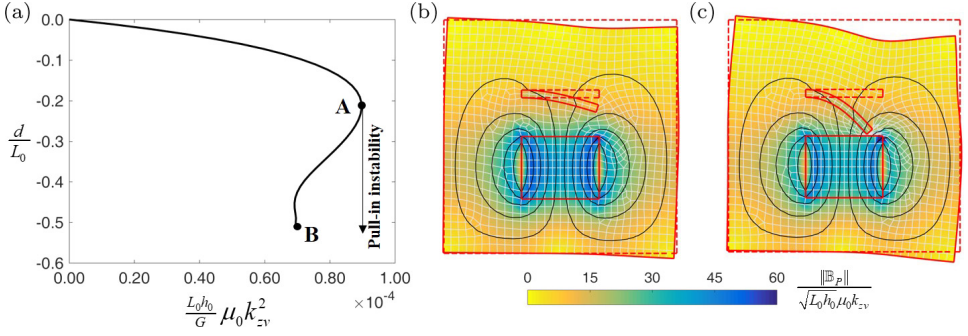


Fig. 12. (a) Evolution of y -directional displacement with respect to the non-dimensional current. (b) and (c) are the configurations at the states of point A and B shown in (a). The relative permeability of the beam is $\mu_r = 1$.

scheme still finds converged results, indicating the robustness of the developed solution scheme.

For the beam in Fig. 10, we set $k_{zv} = 0$ and $\mu_r = 100$, and constrain the displacement at the bottom surface of the beam, i.e., $y = d_0$. Due to higher permeability in the block compared to the free space, it has perturbation on the distribution of magnetic flux produced by the electromagnet (Fig. 13a). The block has a total upward magnetic force nonuniformly distributed at its top surface (Fig. 13b), which leads to larger strain and stress at its two ends and slight thickening of the whole block.

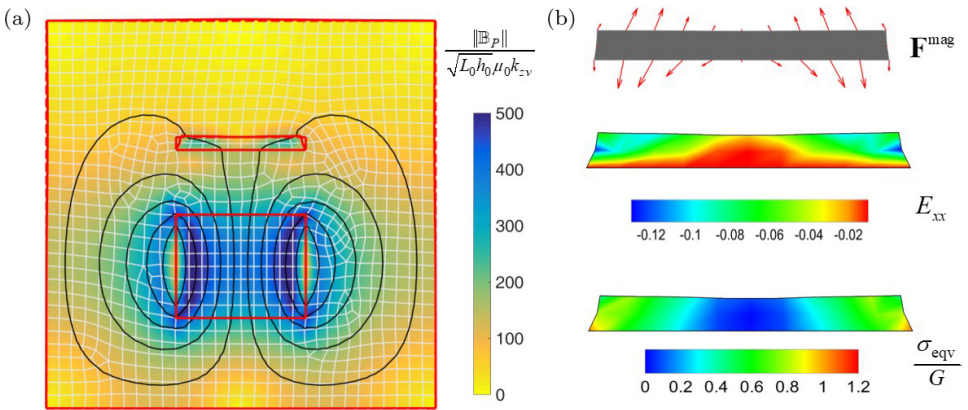


Fig. 13. (a) Distribution of magnetic flux in the deformed configuration at a non-dimensionalized current $\frac{L_0 h_0}{G} \mu_0 k_{zf}^2 = 88$. (b) Distributions of magnetic force, Von Mises stress, and a component of Green strain in the block.

4.5. Snap-through of a current-loading beam

In this example, we have performed a snap-through analysis of a simply supported MAE beam to further demonstrate the efficiency of the developed Riks solution scheme. As shown in Fig. 14, due to the unsymmetrical distribution of current (with respect to the x -axis), the beam shows a self-bending deformation due to the interaction of the current. The relative permeability of the beam is set to be $\mu_r = 100$. The variation of the displacement at the Point P (Fig. 14) shows a snap-through behavior of the beam, as shown in Fig. 15(a), indicating that the beam jumps from configuration at Point A (Fig. 15(b)) to configuration at Point B (Fig. 15(c)) with a much larger bending degree. The magnetic flux in the beam is much larger than that in the free space due to its larger μ_r .

Despite of the ignored inertia effect, it is noted that the model is able to predict the limit point on the equilibrium path where the snap-through or pull-in instability occurs, as shown on the equilibrium path in Figs. 12(a) and 15(a). This is

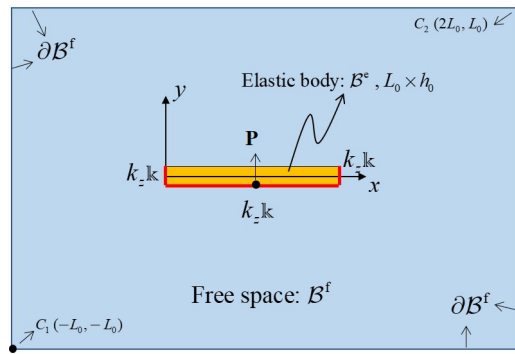


Fig. 14. Schematic of a simply supported beam with a current loading.

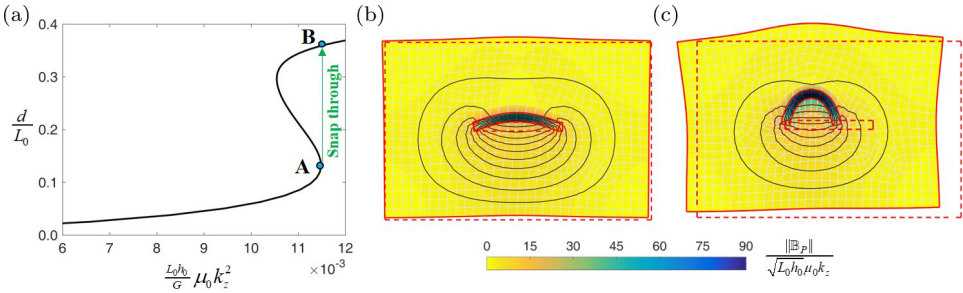


Fig. 15. (a) Evolution of y -directional displacement at point P with respect to the non-dimensional current. (b) and (c) are deformed configurations and distribution of magnetic flux at the state of Point A and Point B shown in (a), respectively.

essentially important because we can identify the critical applied current (or magnetic field) that triggers the shape transition in the process of pull-in instability or snap-through. To model the dynamical process after the instability occurs, the terms related to the inertia effect should be added in the governing equations, and this issue will be studied in our future work.

5. Conclusion

In this work, we have developed a finite element framework to model the strongly coupled mechano-magnetic behaviors focusing on large deformation and instability of slender MAE structures. The magnetic flux is assumed to be an Eulerian quantity measured in the static spatial coordinate system, and thus the Cauchy stress does not directly relate to the magnetic flux. In this way, the mechanical field and magnetic field interact with each other via magnetic forces on the currents and variation of spatial location of body and surface currents. Based on the modified continuum theory, a staggered solution scheme and a Riks method-based scheme have been developed to solve the discretized FE equations, which ensures the variables in both magnetic and mechanical fields are calculated simultaneously. The accuracy and convergence of the model were verified by a 1D MAE bar. Several 2D examples are constructed to demonstrate the efficiency of the model for large deformation and instability of MAE structures within non-uniform magnetic field.

Since the vector potential is used as the unknown in the magnetic field, rather than the scalar potential [Bustamante *et al.*, 2011; Ethiraj and Miehe, 2016], the solution framework can be further extended to 3D MAE with free body currents. Though the developed model has been proved efficient to model large deformation in slender MAE with non-uniform distribution of magnetic field, it is noted that for the interactions between two or multiple MAE objects, the solution scheme may still experience mesh distortion challenges due to the severe deformations of the mesh in the free space. To resolve this issue, two sets of mesh in the simulation may be needed, i.e., static mesh for the analysis of magnetic field in the background space and deformable mesh in MAE to capture its deformation field. The modeling framework may be combined with other advanced constitutive models [Taghizadeh and Darijani, 2018] or temporal-spatial integration algorithms [Li *et al.*, 2018] to simulate realistic magneto-active hydrogels actuators [Li *et al.*, 2019; Liu *et al.*, 2015; Zheng *et al.*, 2018] so as to provide insights for quantitative designs. In addition, experimental verifications for the numerical models are also needed to be performed in particularly for the instability phenomena, which should be considered in future work.

Acknowledgments

This work is partially supported by the start-up fund from Michigan State University and the USDA National Institute of Food and Agriculture, Hatch Project

(No. 1016788). C.C. thanks Prof. Thomas J. Pence from the Department of Mechanical Engineering at MSU for helpful discussion and comment.

References

- Brown, W. F. [1966] *Magnetoelastic Interactions* (Springer, Berlin).
- Bustamante, R., Dorfmann, A. and Ogden, R. W. [2011] “Numerical solution of finite geometry boundary-value problems in nonlinear magnetoelasticity,” *International Journal of Solids and Structures* **48**, 874–883.
- Danas, K. [2017] “Effective response of classical, auxetic and chiral magnetoelastic materials by use of a new variational principle,” *Journal of the Mechanics and Physics of Solids* **105**, 25–53.
- Danas, K. and Triantafyllidis, N. [2014] “Instability of a magnetoelastic layer resting on a non-magnetic substrate,” *Journal of the Mechanics and Physics of Solids* **69**, 67–83.
- Danas, K., Kankanala, S. V. and Triantafyllidis, N. [2012] “Experiments and modeling of iron-particle-filled magnetorheological elastomers,” *Journal of the Mechanics and Physics of Solids* **60**, 120–138.
- Dorfmann, L. and Ogden, R. W. [2016] *Nonlinear Theory of Electroelastic and Magnetoelastic Interactions* (Springer, Boston).
- Erb, R. M., Martin, J. J., Soheilian, R., Pan, C. and Barber, J.R. [2016] “Actuating Soft Matter with Magnetic Torque,” *Advanced Functional Materials* **26**, 3859–3880.
- Eringen, A. C. and Maugin, G. A. [2012] *Electrodynamics of Continua I: Foundations and Solid Media* (Springer, New York).
- Ethiraj, G., and Miehe, C. [2016] “Multiplicative magneto-elasticity of magnetosensitive polymers incorporating micromechanically-based network kernels,” *International Journal of Engineering Science* **102**, 93–119.
- Haldar, K., Kiefer, B. and Menzel, A. [2016] “Finite element simulation of rate-dependent magneto-active polymer response,” *Smart Materials and Structures* **25**, 104003.
- Han, Y., Hong, W. and Faidley, L. [2011] “Coupled magnetic field and viscoelasticity of ferrogel,” *International Journal of Applied Mechanics* **03**, 259–278.
- Han, Y., Hong, W. and Faidley, L. E. [2013] “Field-stiffening effect of magneto-rheological elastomers,” *International Journal of Solids and Structures* **50**, 2281–2288.
- Hou, X., Liu, Y., Wan, G., Xu, Z., Wen, C., Yu, H., Zhang, J. X. J., Li, J. and Chen, Z. [2018] “Magneto-sensitive bistable soft actuators: Experiments, simulations, and applications,” *Applied Physics Letters* **113**, 221902.
- Hu, W., Lum, G. Z., Mastrangeli, M. and Sitti, M. [2018] “Small-scale soft-bodied robot with multimodal locomotion,” *Nature* **554**, 81–85.
- Jackson, J. D. [1999] *Classical Electrodynamics* (Wiley, New York).
- Javili, A., Chatzigeorgiou, G. and Steinmann, P. [2013] “Computational homogenization in magneto-mechanics,” *International Journal of Solids and Structures* **50**, 4197–4216.
- Kalina, K. A., Metsch, P. and Kästner, M. [2016] “Microscale modeling and simulation of magnetorheological elastomers at finite strains: A study on the influence of mechanical preloads,” *International Journal of Solids and Structures* **102–103**, 286–296.
- Kankanala, S. V. and Triantafyllidis, N. [2004] “On finitely strained magnetorheological elastomers,” *Journal of the Mechanics and Physics of Solids* **52**, 2869–2908.
- Keip, M.-A. and Rambašek, M. [2015] “A multiscale approach to the computational characterization of magnetorheological elastomers,” *International Journal for Numerical Methods in Engineering* **107**, 338–360.

- Keip, M.-A. and Rambašek, M. [2017] “Computational and analytical investigations of shape effects in the experimental characterization of magnetorheological elastomers,” *International Journal of Solids and Structures* **121**, 1–20.
- Kim, J., Chung, S. E., Choi, S.-E., Lee, H., Kim, J. and Kwon, S. [2011] “Programming magnetic anisotropy in polymeric microactuators,” *Nature Materials* **10**, 747–752.
- Kim, Y., Yuk, H., Zhao, R., Chester, S. A. and Zhao, X. [2018] “Printing ferromagnetic domains for untethered fast-transforming soft materials,” *Nature* **558**, 274–279.
- Kovetz, A. [2000] *Electromagnetic Theory* (Oxford University Press, Oxford).
- Li, H., Zhang, H., Zheng, Y., Ye, H. and Lu, M. [2018] “An implicit coupling finite element and peridynamic method for dynamic problems of solid mechanics with crack propagation,” *International Journal of Applied Mechanics* **10**, 1850037.
- Li, Z., Huang, R. and Liu, Z. [2019] “A periodic deformation mechanism of a soft actuator for crawling and grasping,” *Advanced Materials Technologies* **4**, 1900653.
- Liu, L. [2014] “An energy formulation of continuum magneto-electro-elasticity with applications,” *Journal of the Mechanics and Physics of Solids* **63**, 451–480.
- Liu, Q., Li, H. and Lam, K. Y. [2018a] “Optimization of deformable magnetic-sensitive hydrogel-based targeting system in suspension fluid for site-specific drug delivery,” *Molecular Pharmaceutics* **15**, 4632–4642.
- Liu, Q., Li, H. and Lam, K. Y. [2018b] “Transition of magnetic field due to geometry of magneto-active elastomer microactuator with nonlinear deformation,” *Journal of Microelectromechanical Systems* **27**, 127–136.
- Liu, Y., Liang, S., Huang, Q., Hu, H., Zheng, Y., Zhang, H. and Shao, Q. [2017] “A robust Riks-like path following method for strain-actuated snap-through phenomena in soft solids,” *Computer Methods in Applied Mechanics and Engineering* **323**, 416–438.
- Liu, Z., Toh, W. and Ng, T. Y. [2015] “Advances in Mechanics of Soft Materials: A Review of Large Deformation Behavior of Hydrogels,” *International Journal of Applied Mechanics* **07**, 1530001.
- Maugin, G. A. [2013] *Continuum Mechanics of Electromagnetic Solids* (Elsevier, Amsterdam).
- Metsch, P., Kalina, K. A., Spieler, C. and Kästner, M. [2016] “A numerical study on magnetostrictive phenomena in magnetorheological elastomers,” *Computational Materials Science* **124**, 364–374.
- Miehe, C., Vallicotti, D. and Teichtmeister, S. [2016] “Homogenization and multiscale stability analysis in finite magneto-electro-elasticity. Application to soft matter EE, ME and MEE composites,” *Computer Methods in Applied Mechanics and Engineering* **300**, 294–346.
- Nedjar, B. [2017] “A coupled BEM-FEM method for finite strain magneto-elastic boundary-value problems,” *Computational Mechanics* **59**, 795–807.
- Pao, Y.-H. [1978] “Electromagnetic forces in deformable continua,” in *Mechanics Today*, ed. S. Nemat-Nasser (Pergamon Press, Oxford, UK), pp. 209–305.
- Pao, Y.-H. and Hutter, K. [1975] “Electrodynamics for moving elastic solids and viscous fluids,” *Proceedings of the IEEE* **63**, 1011–1021.
- Pelteret, J.-P., Davydov, D., McBride, A., Vu, D. K. and Steinmann, P. [2016] “Computational electro-elasticity and magneto-elasticity for quasi-incompressible media immersed in free space,” *International Journal for Numerical Methods in Engineering* **108**, 1307–1342.
- Ponte Castañeda, P. and Galipeau, E. [2011] “Homogenization-based constitutive models for magnetorheological elastomers at finite strain,” *Journal of the Mechanics and Physics of Solids* **59**, 194–215.

- Psarra, E., Bodelot, L. and Danas, K. [2017] “Two-field surface pattern control via marginally stable magnetorheological elastomers,” *Soft Matter* **13**, 6576–6584.
- Rudykh, S. and Bertoldi, K. [2013] “Stability of anisotropic magnetorheological elastomers in finite deformations: A micromechanical approach,” *Journal of the Mechanics and Physics of Solids* **61**, 949–967.
- de Souza Neto, E. A., Perić, D., Dutko, M. and Owen, D. R. J. [1996] “Design of simple low order finite elements for large strain analysis of nearly incompressible solids,” *International Journal of Solids and Structures* **33**, 3277–3296.
- Taghizadeh, D. M. and Darijani, H. [2018] “Mechanical behavior modeling of hyperelastic transversely isotropic materials based on a new polyconvex strain energy function,” *International Journal of Applied Mechanics* **10**, 1850104.
- Vogel, F., Pelteret, J.-P., Kaessmair, S. and Steinmann, P. [2014] “Magnetic force and torque on particles subject to a magnetic field,” *European Journal of Mechanics – A/Solids* **48**, 23–37.
- Yu, K., Fang, N. X., Huang, G. and Wang, Q. [2018] “Magnetoactive Acoustic Metamaterials,” *Advanced Materials* **30**, 1706348.
- Zabihyan, R., Mergheim, J., Javili, A. and Steinmann, P. [2018] “Aspects of computational homogenization in magneto-mechanics: Boundary conditions, RVE size and microstructure composition,” *International Journal of Solids and Structures* **130–131**, 105–121.
- Zhao, R., Kim, Y., Chester, S. A., Sharma, P. and Zhao, X. [2019] “Mechanics of hard-magnetic soft materials,” *Journal of the Mechanics and Physics of Solids* **124**, 244–263.
- Zheng, S., Li, Z. and Liu, Z. [2018] “The fast homogeneous diffusion of hydrogel under different stimuli,” *International Journal of Mechanical Sciences* **137**, 263–270.